

Detection of an ultra-bright submillimeter galaxy in the Subaru/XMM-Newton Deep Field using AzTEC/ASTE

S. Ikarashi^{1*}, K. Kohno^{1,2}, J. E. Aguirre³, I. Artxaga⁴, V. Arumugam⁵,
 J. E. Austermann⁶, J. J. Bock^{7,8}, C. M. Bradford^{7,8}, M. Cirasuolo^{5,9}, L. Earle¹⁰,
 H. Ezawa¹¹, H. Furusawa¹³, J. Furusawa¹³, J. Glenn¹⁰, B. Hatsukade¹², D. H. Hughes⁴,
 D. Iono¹², R. J. Ivison^{5,9}, S. Johnson¹⁴, J. Kamenetzky¹⁰, R. Kawabe¹², R. Lupu³,
 P. Maloney¹⁰, H. Matsuhara¹⁵, P. D. Mauskopf¹⁶, K. Motohara¹, E. J. Murphy⁸,
 K. Nakajima¹⁷, K. Nakanishi¹¹, B. J. Naylor⁷, H. T. Nguyen⁷, T. A. Perera¹⁸,
 K. S. Scott³, K. Shimasaku^{2,17}, T. Takagi¹⁵, T. Takata¹³, Y. Tamura¹², K. Tanaka¹⁹,
 T. Tsukagoshi¹, D. J. Wilner²⁰, G. W. Wilson¹⁴, M. S. Yun¹⁴, J. Zmuidzinas^{7,8}

¹Institute of Astronomy, University of Tokyo, 2-21-1 Osawa, Mitaka, Tokyo 181-0015, Japan

²Research Center for the Early Universe, School of Science, University of Tokyo, 7-3-1 Hongo, Bunkyo, Tokyo 113-0033, Japan

³Department of Physics and Astronomy, University of Pennsylvania, Philadelphia, PA 19104, USA

⁴Instituto Nacional de Astrofísica, Óptica y Electrónica (INAOE), Aptdo. Postal 51 y 216, 72000 Puebla, Pue., Mexico

⁵Institute for Astronomy, University of Edinburgh, Royal Observatory, Blackford Hill, Edinburgh EH9 3HJ, UK

⁶Center for Astrophysics and Space Astronomy, University of Colorado, Boulder, CO 80309, USA

⁷Jet Propulsion Laboratory, Pasadena, CA 91109, USA

⁸California Institute of Technology, Pasadena, CA 91125, USA

⁹UK Astronomy Technology Centre, Royal Observatory, Blackford Hill, Edinburgh EH9 3HJ, UK

¹⁰Dept. of Astrophysical and Planetary Sciences, University of Colorado, 389-UCB, Boulder, CO 80309, USA

¹¹ALMA Project Office, National Astronomical Observatory, 2-21-1 Osawa, Mitaka, Tokyo 181-8588, Japan

¹²Nobeyama Radio Observatory, Minamimaki, Minamisaku, Nagano 384-1305, Japan

¹³Astronomy Data Center, National Astronomical Observatory, Mitaka, Tokyo 181-8588, Japan

¹⁴Department of Astronomy, University of Massachusetts, Amherst, MA 01003, USA

¹⁵Institute of Space and Astronautical Science, Sagamihara, Kanagawa 229-8510, Japan

¹⁶School of Physics & Astronomy, Cardiff University, Queens Buildings, The Parade, Cardiff CF24 3AA, UK

¹⁷Department of Astronomy, University of Tokyo, Hongo 7-3-1, Bunkyo-ku, Tokyo 113-0033, Japan

¹⁸Illinois Wesleyan University 1312 Park Street Bloomington, IL 61701, USA

¹⁹Department of Physics, Faculty of Science and Technology, Keio University, 3-14-1 Hiyoshi, Kohoku-ku, Yokohama, Kanagawa 223-8522, Japan

²⁰Harvard-Smithsonian Center for Astrophysics, 60 Garden Street, Cambridge, MA 02138, USA

Accepted ... ; Received ... ; in original form 2010 September 07

ABSTRACT

We report the detection of an extremely bright (~ 37 mJy at $1100\ \mu\text{m}$ and ~ 91 mJy at $880\ \mu\text{m}$) submillimeter galaxy (SMG), AzTEC-ASTE-SXDF1100.001 (hereafter referred to as SXDF1100.001 or Orochi), discovered in $1100\ \mu\text{m}$ observations of the Subaru/XMM-Newton Deep Field using AzTEC on ASTE. Subsequent CARMA 1300 μm and SMA 880 μm observations successfully pinpoint the location of Orochi and suggest that it has two components, one extended (FWHM of $\sim 4''$) and one compact (unresolved). Z-Spec on CSO has also been used to obtain a wide band spectrum from 190 to 308 GHz, although no significant emission/absorption lines are found. The derived upper limit to the line-to-continuum flux ratio is 0.1–0.3 ($2\ \sigma$) across the Z-Spec band.

Based on the analysis of the derived spectral energy distribution from optical to radio wavelengths of possible counterparts near the SMA/CARMA peak position, we suggest that Orochi is a lensed, optically dark SMG lying at $z \sim 3.4$ behind a foreground, optically visible (but red) galaxy at $z \sim 1.4$. The deduced apparent (i.e., no correction for magnification) infrared luminosity (L_{IR}) and star formation rate (SFR) are $6 \times 10^{13}\ L_{\odot}$ and $11000\ M_{\odot}\ \text{yr}^{-1}$, respectively, assuming that the L_{IR} is dominated by star formation. These values suggest that Orochi will consume its gas reservoir within a short time scale (3×10^7 yr), which is indeed comparable to those in extreme starbursts like the centres of local ULIRGs.

1 INTRODUCTION

Recent rapid advancements in wide and deep surveys at millimeter/submillimeter (mm/submm) wavelengths have led to successive discoveries of numerous mm/submm-bright galaxies (SMGs) in the early universe.

After the pioneering works performed with the SCUBA (Cunningham et al. 1994; Holland et al. 1999) on the JCMT 15 m telescope (e.g., Smail et al. 1997; Hughes et al. 1998; Eales et al. 1999; Ivison et al. 2000), numerous mapping surveys at $\lambda = 850 \mu\text{m}$ have been conducted toward blank fields (e.g., Borys et al. 2003; Coppin et al. 2006; Pope et al. 2006) and over-dense regions (e.g., Stevens et al. 2003; Knudsen et al. 2006). MAMBO (Kreysa et al. 1998) on the IRAM 30 m telescope and BOLOCAM (Laurent et al. 2005) on the CSO 10 m have also been used to obtain 1200 $\mu\text{m}/1100 \mu\text{m}$ images of blank fields (Greve et al. 2004, 2008; Bertoldi et al. 2007; Laurent et al. 2005) and over-dense regions (e.g., Greve et al. 2007).

A new mm-wavelength bolometer camera, AzTEC for 1100 μm (Wilson et al. 2008a), was mounted on JCMT and produced wide-area (\sim a few 100–1000 arcmin 2 scale) images of well studied fields such as COSMOS (Scott et al. 2008), GOODS-N (Perera et al. 2008), Lockman hole, SXDF (Austermann et al. 2010), and over-dense regions (Wardlow et al. 2010).

New submm wave telescopes in northern Chile, i.e., ASTE 10 m and APEX 12 m telescopes, are now also equipped with bolometer cameras, i.e., AzTEC for 1100 μm and LABOCA for 870 μm (Siringo et al. 2008). Owing to the very suitable atmospheric conditions of the site, these telescopes routinely obtain wide-area images of various fields such as SSA22 (Tamura et al. 2009), ECDFS/GOODS-S (Weiß et al. 2009; Scott et al. 2010), ADF-S (Hatsukade et al. 2011), a proto-cluster (Beelen et al. 2008) and a cluster (Wilson et al. 2008b). A wider area (\sim 10 deg 2 scale) short submm survey has been conducted with BLAST (Devlin et al. 2009), and \sim 100 deg 2 scale mm/submm surveys are now coming using SPT (Vieira et al. 2010) and Herschel (Amblard et al. 2010; Eales et al. 2010).

One of the important findings from these recent mm/submm surveys is the detection of ultra-bright populations of SMGs and it is predicted that this ultra-bright population is probably lensed by foreground clusters and/or massive galaxies (e.g., Blain 1996; Negrello et al. 2007). For instance, an ultra-bright mm/submm galaxy, MM J065837-5557.0, with a flux density of \sim 20 mJy at 1100 μm (Wilson et al. 2008b) and \sim 48 mJy at 870 μm (Johansson et al. 2010) has been detected near the center of the Bullet cluster ($z = 0.297$). This source, whose brightness appears to be highly boosted ($>$ 20–75) by gravitational lensing, is a luminous infrared galaxy (LIRG) behind the Bullet cluster at $z \sim 2.79$ (Johansson et al. 2010; Gonzalez et al. 2010). A similar but brighter source has also been reported toward the cluster MACS J2135-010217 ($z = 0.325$). SMM J2135-0102 has an 870 μm flux density of 106 mJy, and is an ultra-luminous IR galaxy (ULIRG) at a spectroscopically confirmed redshift of 2.33 and with an amplification factor of \sim 33 (Swinbank et al. 2010; Ivison et al. 2010a). Owing to the strong magnification of the gravitational lens, these lensed SMGs provide a unique opportunity to understand the physical properties of extreme star-

formation in the early universe even with existing telescopes (Swinbank et al. 2010). Furthermore, SPT surveys have shown that ultra-bright submm/mm galaxies exist in some surface density; 20 dust-dominated SMGs above 10 mJy at 1.4 mm were detected in 87 deg 2 area (Vieira et al. 2010). The 14.4 deg 2 survey with Herschel, as a part of the H-ATLAS project, uncovered 11 bright 500 μm sources ($>$ 100 mJy at 500 μm) within the survey area, and 5 of 11 have been identified as lensed, dusty starburst galaxies at $z = 1.6 - 3.0$ (Negrello et al. 2010). Large mm/submm surveys enable us to find these new populations.

Here, we report a serendipitous detection of an ultra-bright SMG in the Subaru/XMM-Newton Deep Field (SXDF), termed as AzTEC-ASTE-SXDF1100.001 (hereafter referred to as SXDF1100.001) or Orochi¹, during a course of wide and deep 1100 μm surveys using AzTEC mounted on ASTE.

This paper is organized as follows. The AzTEC on ASTE detection is reported in section 2, and subsequent CARMA and SMA observations are described in section 3, along with the multi-wavelengths images from optical/infrared to radio. Spectroscopic observations using Z-Spec on CSO are discussed in section 4. The modeling of the SED and derived physical properties, including discussions on the source size/structure and implications for star formation properties of Orochi are given in section 5.

Throughout this paper, we adopt a cosmology with density parameters $\Omega_\Lambda = 0.7$ and $\Omega_M = 0.3$ and the Hubble constant $H_0 = 70 \text{ km s}^{-1} \text{ Mpc}^{-1}$.

2 AZTEC/ASTE 1100 μm OBSERVATIONS AND RESULTS

2.1 AzTEC/ASTE observations

We conducted 1100 μm imaging observations of a cluster of Ly α Emitters (LAEs) at $z \sim 5.7$ (Clump B; Ouchi et al. 2005) in SXDF using the AzTEC camera (Wilson et al. 2008a) mounted on ASTE (Ezawa et al. 2004, 2008), from November 26 to December 21, 2008. The observations were carried out remotely from the ASTE operation rooms through the network observation system N-COSMOS3 developed by the National Astronomical Observatory of Japan (NAOJ) (Kamazaki et al. 2005). The full width at half maximum (FWHM) of the AzTEC beam on ASTE is 30'' at 1100 μm , and the field of view of the array is roughly circular with a diameter of 8''. During the ASTE 2008 observation run, 117 of 144 AzTEC detectors were operational.

We imaged a \sim 6.6' diameter circular field of Clump B, centered at R.A. (J2000) = $02^h 18^m 19.60^s$, Dec. (J2000) = $-5^\circ 32' 52''.0$. We used a Lissajous scan pattern (Wilson et al. 2008b) in order to maximize the observation efficiency. We selected a maximum velocity of 300'' s $^{-1}$ in order to mitigate low-frequency atmospheric fluctuations. We obtained a total of 39 individual observations for Clump B, taking \sim 40 min for each observation. The atmospheric zenith opacity at 220 GHz was $\tau_{220\text{GHz}} = 0.017 - 0.100$ as monitored with a radiometer at the ASTE telescope site.

¹ a Japanese word referring to an ancient Japanese legendary monster.

Table 1. AzTEC on ASTE observations.

Parameters	Values
Observation date	Nov. 26 - Dec. 21, 2008
Wavelength/Frequency	1100 μm /270 GHz
Bandwidth	50 GHz
Number of detectors	144 (total), 117 (operational)
Beam size (FWHM)	30''
Field center (J2000)	R.A. = $02^h18^m19.59^s$ Dec. = $-05^\circ32'52''.00$
Field area	136 arcmin ² (50 %-coverage region)
Map noise level	0.6–1.0 mJy
Pointing source	J0132–169
Flux calibrator source	Uranus, Neptune
Opacity at 220 GHz	0.017–0.100

Uranus or Neptune were observed at least once a night in order to measure each detector's point spread function (PSF) and relative position and to determine the flux conversion factor for absolute calibration (Wilson et al. 2008a). Pointing observations with the quasar J0132–169 were performed every 2h across observations for Clump B; the resultant pointing accuracy is better than 3'' (Wilson et al. 2008b). A pointing model is devised by interpolating these pointing data temporally and is applied to the astrometry for correction of pointings. Observational information is summarized in Table 1.

2.2 AzTEC Data Reduction

The data were reduced using the AzTEC data reduction pipeline written in the Interactive Data Language (IDL) in a manner similar to that in Scott et al. (2008). Here, we provide a brief summary of the process and point out the difference. The data were divided into 15 s intervals of time-series data. Spikes were then removed from the time-series data. A principal component analysis (PCA) method was used to subtract the sky emission, and the effect of PCA cleaning on the point source response is traced by reducing synthetic, noiseless time-series data with a simulated point source using the same approach that employed for the actual data. This ‘point source kernel’ is indicative of the effect of PCA on the point source profile and flux attenuation of real point sources in the map and we corrected flux densities of AzTEC sources based on this kernel (Downes et al. 2011). The cleaned time-series data were projected into a map space using 3'' \times 3'' pixels, and the 39 individual observations were co-added into a single map by weighted averaging. We also created 100 synthesised noise realizations by randomly multiplying each 15 s time-series interval by ± 1 (similar to the ‘scan-by-scan’ jackknifing technique used in Scott et al. (2008)). These noise realizations are free of astronomical signals, including the signals from confused sources in the map. The co-added map and the 100 noise realizations were optimally filtered for the detection of point sources.

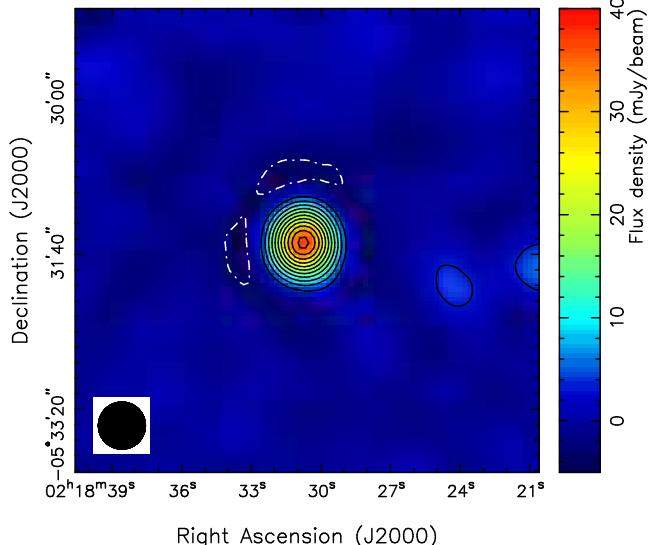


Figure 1. The AzTEC/ASTE 1100 μm image of Orochi. The contour levels are 5, 10, 15, 20, 25, 30, 35, 40, 45, 50 and 55 σ , where $1 \sigma = 0.65 \text{ mJy beam}^{-1}$. Negatives are shown in white contours.

2.3 AzTEC 1100 μm results

The achieved average noise level of the resulting map is 0.60–1.00 mJy over a 136 arcmin² area. We found an ultra bright source, Orochi, at $\alpha(\text{J2000}) = 02^h18^m30.68^s$ and $\delta(\text{J2000}) = -05^\circ31'31''.37$. The flux density at 1100 μm is $37.28 \pm 0.65 \text{ mJy}$. The 1100 μm image of Orochi is shown in Fig. 1. The source size is consistent with the point source kernel or PSF of the AzTEC/ASTE observations. Hence, the point source kernel is understood as the AzTEC/ASTE beam. The estimated position errors from AzTEC signal-to-noise ratio and the beam size are 0''.9 (1 σ) and 1''.4 (2 σ).

3 INTERFEROMETRIC IDENTIFICATION AND MULTI WAVELENGTH PROPERTIES

We performed interferometric imaging with CARMA and SMA of Orochi to constrain its position. With the refined position estimate, we searched the literature and the archives for multi-wavelength data.

3.1 CARMA 1300 μm observations and results

3.1.1 CARMA 1300 μm Observations & Reduction

We conducted follow-up observations of Orochi on August 16, 2009, using the D configuration with 15 antennas of the CARMA. The phase centre was $\alpha(\text{J2000}) = 02^h18^m21^s$ and $\delta(\text{J2000}) = -05^\circ31'31''$. The projected baseline lengths ranged from 10 m to 108 m. The CARMA correlator was configured to cover a 1.5 GHz width in each sideband, yielding a total bandwidth of 3 GHz for continuum observations after adding the two sidebands. The centre frequency of the receivers was tuned to 230 GHz. We observed a bright QSO, J0108+015 (18.8° away from Orochi) as a visibility calibrator and Uranus as a flux calibrator. To obtain an empirical

Table 2. CARMA observations.

Parameters	Values
Observation date	Aug. 16, 2009
Wavelength/Frequency	1300 μm /232 GHz
Bandwidth	1.5 GHz
Phase center (J2000)	R.A. = $02^h 18^m 21^s$ Dec. = $-05^\circ 31' 31''$
Phase calibrator	J0108+015
Flux calibrator	Uranus
Array configuration	D configuration
projected baseline	10–108 m
Primary beam	$35''.4$ (FWHM)
Synthesized Beam size	$3''.2 \times 2''.1$ (P.A.= -16.4°)
Map noise level	1.3 mJy
Opacity at 230 GHz	0.1–0.3

upper limit on the systematic position error induced by baseline errors, we observed a radio galaxy, J0241-082 (25° away from the visibility calibrator; the distance is approximately 1.33 times that between Orochi and the visibility calibrator) during a track. We observed a bright QSO, 3C84, as a bandpass calibrator. The raw CARMA data were calibrated and imaged with natural weight using MIRIAD (Sault et al. 1995). We found that the quality of the data from the upper side band (USB) was significantly poorer than that of the lower side band (LSB) data. Therefore, we used only the LSB data for pinpointing the position of Orochi and subsequent analysis. Observational information is summarized in Table 2.

3.1.2 CARMA 1300 μm results

We find a source with 11σ significance at $\alpha(J2000) = 02^h 18^m 30.67^s$ and $\delta(J2000) = -05^\circ 31' 31''.42$ (Fig. 2). The CARMA 1300 μm source position coincides well with that of the centroid of the AzTEC/ASTE 1100 μm source. The derived source position is shown in Table 3.

To evaluate the reliability of the astrometry in our CARMA observations, we estimate the statistical errors due to the noise obtained in fitting a point source to the calibrated visibilities and systematic errors due to uncertainties in interferometer baselines. Details of these analysis followed Younger et al. (2007). The derived statistical errors are shown in Table 3. The systematic astrometry error caused by baseline length uncertainties is estimated as $\sim 0''.5$ based on the CARMA image of a known radio source J0241-082. The estimated statistical positional errors for RA and Dec are $0''.09$ and $0''.12$.

3.2 SMA 880 μm observations and results

3.2.1 SMA 880 μm Observations & Reduction

We conducted follow-up observations of Orochi on December 10, 2009, using the compact configuration with 8 antennas of the SMA. The phase center was $\alpha(J2000) = 02^h 18^m 22^s$ and $\delta(J2000) = -05^\circ 31' 35''$. The projected baseline lengths ranged from 7 m to 70 m. The SMA correlator was equipped with 4.0 GHz in each sideband, providing a total of 8

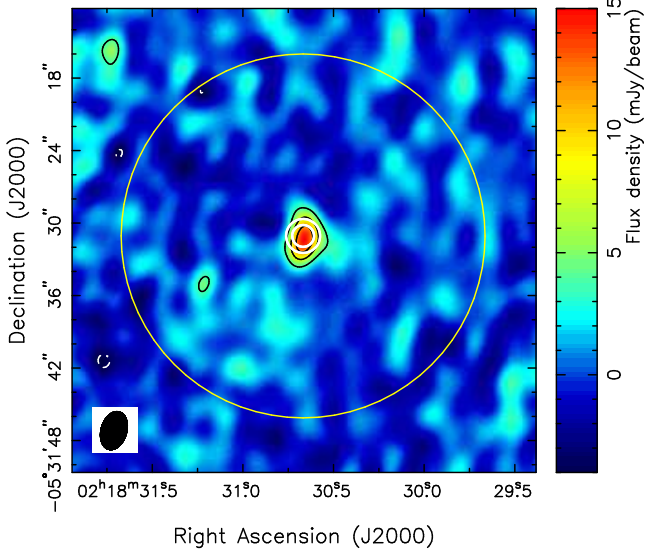


Figure 2. The CARMA 1300 μm image of Orochi. The contour levels are 3 , 6 , and 9σ ($1\sigma = 1.3$ mJy). Negatives are shown in white contours. The synthesized beam is shown on the lower left. Note that no correction of the primary beam attenuation was made in this map. The large solid yellow circle shows the beam size of AzTEC/ASTE (30''). The small solid white circles show the estimated position errors; the inner one shows 1σ error ($0''.9$) and the outer one shows 2σ error ($1''.4$).

Table 4. SMA observations.

Parameters	Values
Observation date	Dec. 10, 2009
Wavelength/Frequency	880 μm / 340 GHz
Bandwidth	8 GHz
Phase center (J2000)	R.A. = $02^h 18^m 22^s$ Dec. = $-05^\circ 31' 35''$
Phase calibrator	J0132-169
Flux calibrator	Uranus
Array configuration	compact configuration
projected baseline	7–70 m
Primary beam	$32''.4$ (FWHM)
Synthesized Beam size	$3''.0 \times 1''.9$ (P.A.= 8.1°)
Map noise level	2.2 mJy
Opacity at 225 GHz	0.1–0.3

GHz bandwidth for continuum observations. The centre frequency of the receivers was tuned to 340 GHz. We observed a bright QSO, J0132-169 (16.0° away from Orochi) as a visibility calibrator and Uranus as a flux calibrator. To obtain an empirical upper limit on the systematic position error induced by baseline errors, we observed a radio galaxy, J0238-166 (22.7° away from the visibility calibrator; the distance is approximately 1.4 times that between Orochi and the visibility calibrator) during a track. We observed a bright QSO, 3C454.3, and Callisto as bandpass calibrators during the track.

The raw SMA data were calibrated using the MIR package (Scoville et al. 1993). Imaging was carried out in MIRIAD with natural weighting. Observational information is summarized in Table 4.

Table 3. Peak positions and their errors for VLA 20 cm, CARMA 1300 μm , AzTEC 1100 μm , SMA 880 μm , and Subaru z' -band images of Orochi. The measured offsets from the z' -band peak position are also listed.

image	$\alpha(\text{J2000})$	$\delta(\text{J2000})$	$\sigma(\alpha)$ (arcsec)	$\sigma(\delta)$ (arcsec)	$\sigma'(\alpha)^a$ (arcsec)	$\sigma'(\delta)^a$ (arcsec)	z' -band offset $\sigma(\alpha)$ (arcsec)	z' -band offset $\sigma(\delta)$ (arcsec)
VLA	02 ^h 18 ^m 30.67 ^s	-05°31'31".48	0.07	0.09	0.26	0.23	-0.18	0.32
CARMA	02 ^h 18 ^m 30.67 ^s	-05°31'31".28	0.09	0.12	0.27	0.24	-0.18	0.52
AzTEC	02 ^h 18 ^m 30.67 ^s	-05°31'30".97	0.9	0.9	0.9	0.9	-0.18	0.83
SMA	02 ^h 18 ^m 30.68 ^s	-05°31'31".68	0.04	0.06	0.25	0.22	0.00	0.12
z' -band	02 ^h 18 ^m 30.68 ^s	-05°31'31".80	0.25	0.21	-	-	-	-

^a denotes the combined (z' plus radio or submm/mm) 1 σ uncertainty in position.

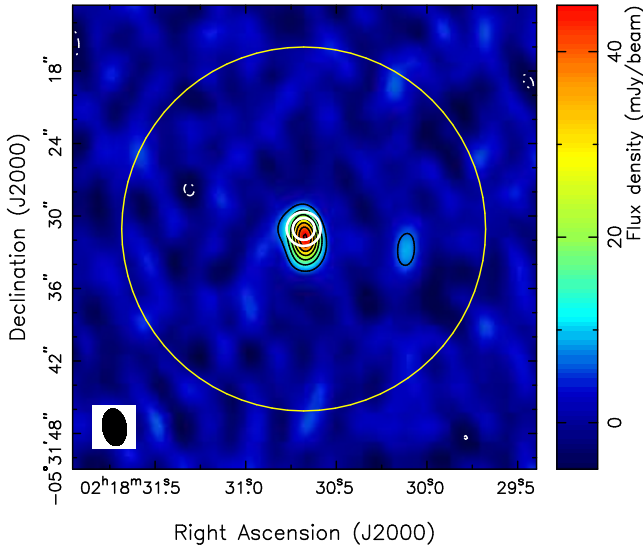


Figure 3. The SMA 880 μm image of Orochi. The contour levels are -3, 3, 6, 9, 12, 15, 18, and 21 σ ($1 \sigma = 2.2 \text{ mJy}$). Negatives are shown in white contours. The synthesized beam is shown on the lower left. Note that no correction of the primary beam attenuation was made in this map. The large solid yellow circle shows the beam size of AzTEC/ASTE (30''). The small solid white circles show the estimated position errors; the inner one shows 1 σ error (0''.9) and the outer one shows 2 σ error (1''.4).

3.3 Multi-wavelength Data

We find a multi-wavelength counterpart at the CARMA/SMA position using optical, near-infrared (NIR), mid-infrared (MIR), and radio wavelengths from archival data. The derived flux and corresponding images are displayed in Table 5 and Fig. 4, respectively. Here, we briefly describe the archival data. Optical data in 5 broad-bands, B , V , Rc , z' , and i' -band, were provided by the SXDS project data release 1 (Furusawa et al. 2008). A u_R -band image was obtained from the SMOKA archive in Japan. K -band and J -band images were provided by UKIDSS/UDS surveys data release 1 (Warren et al. 2007). Infrared data in all four Spitzer IRAC bands (3.6, 4.5, 5.8, and 8 μm) are available from the SWIRE survey, and the MIPS band (24 μm) is available from the SpUDS survey. These data were obtained from the Spitzer archive. Orochi was detected in a 20 cm VLA image and catalogued as VLA J021830-05315 (Simpson et al. 2006). An updated VLA image, taken in the A-configuration (Arumugam et al., in prep.), has been incorporated into the multi-wavelengths dataset. Unfortunately, the counterpart of Orochi is not isolated on the 24 μm image. Other infrared bright source is located in south west of Orochi and it looks like an extended source in the optical wavelength images (Fig. 4). Therefore, we regard the aperture photometry data in the SWIRE catalogue as an upper limit. The photometry data at 1000, 1100, 1200, 1300, 1400, and 1500 μm are obtained from Z-Spec observations. See section 4 for details.

4 Z-SPEC 1500 μM TO 1000 μM ULTRA-WIDEBAND SPECTROSCOPY

4.1 Observations and data reduction

In order to determine the redshift of Orochi, we searched for redshifted molecular/atomic lines using Z-Spec, a single-beam grating spectrometer which disperses the 190–308 GHz (or 1570–970 μm) band across a linear array of 160 bolometers (Bradford et al. 2009, and references therein). The resolving power (R) runs from 250 to 300, from the highest end to the lowest end of the band. This gives a frequency resolution of $\sim 700 \text{ MHz}$ or a velocity resolution of $\sim 880 \text{ km s}^{-1}$ at the centre of the band ($\sim 240 \text{ GHz}$).

Orochi was observed for six nights during late November to early December of 2009 using Z-Spec mounted on the Caltech Submillimeter Observatory (CSO) 10 m telescope. A traditional chop-and-nod mode, with the secondary chopping at 1.6 Hz and a nod period of 20 s, was adopted.

3.2.2 SMA 880 μm results

We find a source with 21 σ significance at the position of $\alpha(\text{J2000}) = 02^{\text{h}}18^{\text{m}}30.67^{\text{s}}$ and $\delta(\text{J2000}) = -05^{\circ}31'31".68$ (Fig. 3). The SMA 880 μm source position coincides with that of the centroid of the AzTEC/ASTE 1100 μm source and CARMA 1300 μm source. The derived source positions of AzTEC/ASTE, CARMA, and SMA are shown in Table 3 along with the VLA source position.

The systematic astrometry error of the SMA source caused by baseline length uncertainties was estimated as $\sim 0''.1$ based on the SMA image of J0238-166. The estimated statistical positional errors for RA and Dec are 0''.04 and 0''.06.

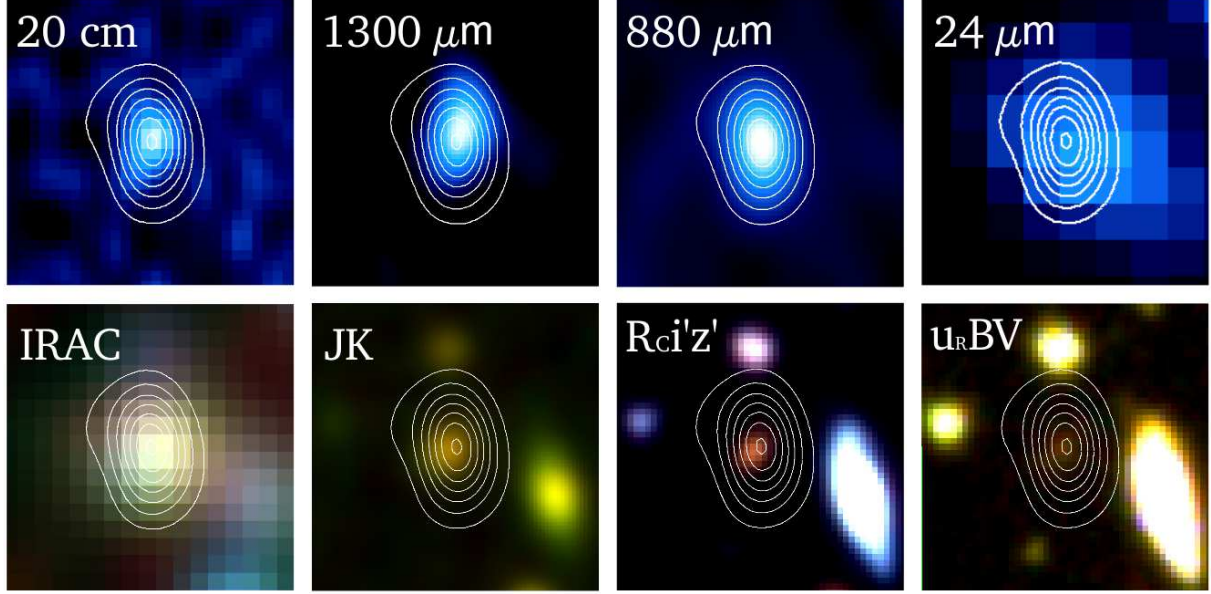


Figure 4. Multi-wavelength images of Orochi with SMA contours (3, 6, 9, 12, 15, 18, and 21 σ). The size of each image is $10'' \times 10''$; north is towards the top of the image and east is towards the left side of the image. From left to right and top to down: VLA 20 cm; CARMA 1300 μm ; SMA880 μm ; MIPS 24 μm ; rgb image of IRAC/ch1 (blue), ch2 (green), ch3 and ch4 (red); rg image of WFCAM/J (green) and K (red); rg image of SuprimeCam/R, i' and z' ; rgb image of SuprimeCam/ u_R , B and V .

Table 5. Flux densities of Orochi.

Wavelength	Camera/Telescope	Magnitude/Flux	Reference
4.5 – 10 keV	EPIC/XMM-Newton	$< 5 \times 10^{-15} (\text{erg/cm}^2/\text{s})^a$	Ueda et al. (2008)
0.5 – 4.5 keV	EPIC/XMM-Newton	$< 8 \times 10^{-16} (\text{erg/cm}^2/\text{s})^a$	Ueda et al. (2008)
0.380 μm (u_R -band)	SuprimeCam/Subaru	$< 26.76 (m_{AB})^b$	-
0.445 μm (B -band)	SuprimeCam/Subaru	$25.86 \pm 0.05 (m_{AB})$	Furusawa et al. (2008)
0.551 μm (V -band)	SuprimeCam/Subaru	$25.51 \pm 0.05 (m_{AB})$	Furusawa et al. (2008)
0.659 μm (Rc -band)	SuprimeCam/Subaru	$24.80 \pm 0.05 (m_{AB})$	Furusawa et al. (2008)
0.771 μm (i' -band)	SuprimeCam/Subaru	$23.68 \pm 0.05 (m_{AB})$	Furusawa et al. (2008)
0.922 μm (z' -band)	SuprimeCam/Subaru	$22.88 \pm 0.05 (m_{AB})$	Furusawa et al. (2008)
1.215 μm (J -band)	WFCAM/UKIRT	$0.0096 \pm 0.00066 (\text{mJy})$	Warren et al. (2007)
2.179 μm (K -band)	WFCAM/UKIRT	$0.0224 \pm 0.0017 (\text{mJy})$	Warren et al. (2007)
3.6 μm	IRAC/ <i>Spitzer</i>	$0.046 \pm 0.0018 (\text{mJy})$	-
4.5 μm	IRAC/ <i>Spitzer</i>	$0.057 \pm 0.0017 (\text{mJy})$	-
5.8 μm	IRAC/ <i>Spitzer</i>	$0.075 \pm 0.0088 (\text{mJy})$	-
8 μm	IRAC/ <i>Spitzer</i>	$0.110 \pm 0.013 (\text{mJy})$	-
24 μm	MIPS/ <i>Spitzer</i>	$< 0.384 (\text{mJy})$	-
70 μm	MIPS/ <i>Spitzer</i>	$< 12 (\text{mJy})^c$	-
160 μm	MIPS/ <i>Spitzer</i>	$< 72 (\text{mJy})^c$	-
880 μm	-/SMA	$90.7 \pm 2.2 \pm 20.7^d (\text{mJy})$	This work
1000 μm	Z-SPEC/CSO	$51.9 \pm 1.2 (\text{mJy})$	This work
1100 μm	AzTEC/ASTE	$37.3 \pm 0.7 (\text{mJy})$	This work
1100 μm	Z-SPEC/CSO	$38.4 \pm 0.9 (\text{mJy})$	This work
1200 μm	Z-SPEC/CSO	$31.3 \pm 0.8 (\text{mJy})$	This work
1300 μm	-/CARMA	$24.6 \pm 1.3 \pm 5.3^d (\text{mJy})$	This work
1300 μm	Z-SPEC/CSO	$23.9 \pm 1.0 (\text{mJy})$	This work
1400 μm	Z-SPEC/CSO	$19.5 \pm 0.9 (\text{mJy})$	This work
1500 μm	Z-SPEC/CSO	$13.9 \pm 1.2 (\text{mJy})$	This work
20 cm	-/VLA	$0.238 \pm 0.038 (\text{mJy})$	Arumugam et al., in prep
50 cm	-/GMRT	$0.315 \pm 0.120 (\text{mJy})$	Dunne et al. (2009)

^a indicates the detection limit in Ueda et al. 2008 and corresponds to a confidence level of 99.91%.

^b indicates the detection limit with 2 σ and aperture size of 2'' (diameter).

^c indicates the upper limit with 3 σ .

^d indicates the uncertainty of uv model fitting for the extended structure. See section 5.1 for details.

Table 6. Z-Spec observations.

Observation date	Values
Observation date	Nov.–Dec., 2009
Wavelength/Frequency	970–1570 μm / 190–308 GHz
Spectral resolution	~ 700 MHz at 240 GHz
Flux calibrator	Mars
Averaged noise level	~ 2.7 mJy
Opacity at 225 GHz	0.03–0.17

The total integration time was 16 h, excluding bad scans (showing unreasonable baseline shape and/or offset). The absolute intensity scale was calibrated from observations of Mars, with a channel-to-channel correction based on quasar spectra measured during the observation run. The overall calibration uncertainties are estimated to be less than 10%, except at the lowest frequencies which are degraded by the wing of the 186 GHz atmospheric water line. The Z-Spec observations are summarized in Table 6.

4.2 Z-Spec result

The derived Z-Spec spectrum of Orochi is displayed in Fig. 5. Continuum emission is detected across the whole band, and the S/N ratio exceeds 10 above ~ 220 GHz. The averaged noise level of the spectrum is 2.7 mJy. We found a clear slope of continuum emission, which is attributed to the thermal dust emission. The best-fit continuum spectrum across the Z-Spec band is

$$F_\nu = (30.1 \pm 0.5) \left(\frac{\nu}{250 \text{ GHz}} \right)^{3.00 \pm 0.11} \text{ mJy.} \quad (1)$$

Considering absolute flux calibration errors of 10–20% in the mm wavelength band, the measured flux densities with SMA and CARMA coincide well with the Z-Spec continuum flux. We derived the average flux densities at 1000, 1100, 1200, 1300, 1400, and 1500 μm by binning the Z-Spec spectrum into bands of width ~ 7 GHz. The results are listed in Table 5.

We see no significant emission/absorption line feature across the band, and therefore we were unable to determine the redshift of Orochi from these Z-Spec data. For a more quantitative analysis, we use the redshift-finding algorithm described in Lupu et al. (in preparation.), which computes the average S/N ratio from all CO, [CI], [CII], and [NII] transitions falling into the Z-Spec bandpass as a function of redshift. The resulting redshift probability function is very noisy, and the average S/N ratio at all redshifts is < 3 sigma, demonstrating the lack of significant line emission in these data.

The upper limits on the expected CO emission lines and their implications are discussed in section 5.

5 DISCUSSION

In this section, we discuss the properties of Orochi, an ultra-bright SMG identification in AzTEC/ASTE surveys and confirmed by subsequent CARMA/SMA observations.

First, the source structure is; the discovery of the spatially extended submm/mm bright component accompanied with an unresolved compact bright source is discussed. Then, detailed modeling of SEDs as well as the derivations of physical quantities are presented. We suggest that an ultra-bright SMG at a redshift of ~ 3.4 has been discovered just behind a red foreground galaxy at $z \sim 1.4$ and that Orochi is likely to be lensed by the foreground galaxy.

The deduced star formation properties and internal structures of Orochi are also discussed, along with their implications.

5.1 Discovery of the extended bright structure in Orochi

We find that Orochi is spatially resolved and that it has two components—an extended structure and a compact unresolved one—from the analysis of the visibility amplitude as a function of the projected baseline length in SMA data (Fig. 6). The plot of the phase calibrator is almost constant, whereas the visibility amplitude of Orochi appears to reduce significantly for a longer uv-distance. The visibility amplitude was fitted with a combination of a Gaussian (FWHM of $4''.0$) and an unresolved point source. This fitting was carried out using the uvfit task in MIRIAD. The estimated flux densities of the extended and compact structures are 33.7 ± 16.2 mJy and 38.9 ± 3.2 mJy, respectively; in other words approximately a half of the total $880 \mu\text{m}$ flux (~ 73 mJy) is originated from the extended component. Note that the flux densities of the extended component and the unresolved component are 42.1 ± 20.3 mJy and 48.6 ± 4.0 mJy, respectively, after applying a correction of the primary beam response².

On the VLA image, Orochi is spatially resolved with a size of $1''.84 \times 0''.95$ at PA 23.9° . A single source model

² In order to confirm the existence of the extended component, we carried out imaging of the extended component from the residual data after subtracting the unresolved component in uv domain. For this imaging, we used uv data at uv-distance = $10 - 30$ $k\lambda$ in order to achieve better signal-to-noise ratio. The image achieves the noise level of 4.1 mJy and the synthesized beam size of $4''.8 \times 4''.3$ (P.A.= 84°). We found a point source on the residual image and its flux density is 20.8 ± 4.1 mJy. This flux density is consistent with the estimated flux density at uv-distance of $10 - 30$ $k\lambda$ on the visibility amplitude plot, 18.9 ± 4.8 mJy (Fig. 6). In applying primary beam correction for Orochi, the effect of the extended source size should be considered, because Orochi is located 9 arcsec away from the phase centre of SMA. The primary beam response is 0.80 at the center of the source position, 0.87 at the inner edge of the extended components, and 0.73 at the outer edge of the extended components. This means that the effect of primary beam correction for the extended components depends on its structure. In order to evaluate this effect, we applied primary beam correction for the residual image. Considering the fact that the extended component is unresolved in the beam size of this map ($\sim 4''.7$), the corrected flux density on the residual image is equivalent to the corrected flux density of the extended component. The corrected flux density of the residual image is 25 mJy, which is equivalent to applying the primary beam response of 0.8, therefore we can apply the primary beam response of 0.8 to the extended component.

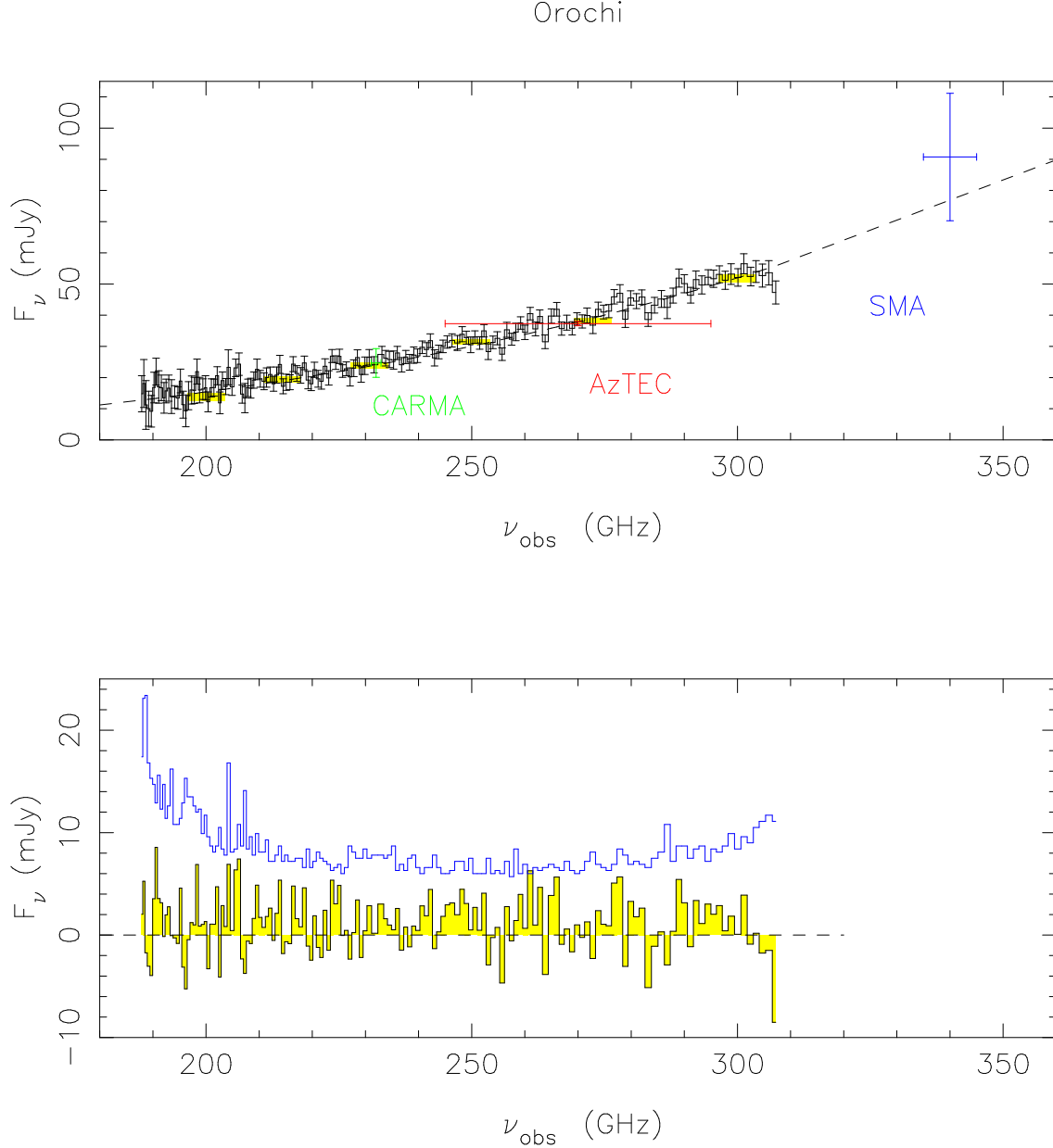


Figure 5. The Z-Spec mm-wavelength spectrum of Orochi. The top panel shows observed flux density by Z-Spec. The dotted line is the fitted continuum, $S \propto \nu^{3.00 \pm 0.11}$. The blue, red and green data points show the flux densities and error bars (without absolute calibration error) measured with the SMA, AzTEC/ASTE, and CARMA, respectively. The horizontal bars give the bandwidth. The yellow box shows areas used for calculating the continuum flux densities in Table 5. The bottom panel shows the Z-Spec spectrum after subtracting continuum flux. The yellow histogram shows the residual spectrum of Orochi and the blue histogram shows the 3σ errors.

with this VLA source size can also fit the data, but the two-component model provides a better fit (Fig. 6). The exact reason for the difference between the source size determined via our VLA and SMA data is not clear. The VLA image published by Simpson et al. (2006) was made with visibilities from the VLA’s DnC and B configurations and yields a flux only $30 \mu\text{Jy}$ ($\sim 10\%$, and $< 1\sigma$) below the deeper VLA image used here (Arumugam et al., in prep), which supplements the Simpson et al. data with visibilities from A configuration. It is unlikely, therefore, that any loss of sig-

nificant extended structure is due to the uv coverage. It is possible that the radio-to-submm flux ratio varies across the structure: a dust temperature gradient may produce such a difference, because a lower dust temperature results in a lower radio flux density, based on the radio-FIR correlation (e.g., Condon 1992; Ivison et al. 2010b) as shown in Fig. 12. It is also possible that faint, compact AGN-related emission may influence the radio morphology, leading to a smaller apparent size. It is clear that more sensitive submm and radio imaging is required to address the issue conclusively.

This two-component feature can also be observed in the CARMA 1300 μm image (Fig. 7), although the signal-to-noise ratio of the CARMA data is worse than that of the SMA data. We conducted two-component fittings of the CARMA data as we did for the SMA data. The resultant source size of the extended component on the CARMA data is $\sim 2''.7$ (FWHM). The estimated flux densities of the extended and compact structures are 8.5 ± 3.5 mJy and 11.4 ± 2.5 mJy, respectively, and the total flux density is ~ 20 mJy at 1300 μm (Table 7). We also applied primary beam correction for CARMA image using a primary beam response of 0.81, as we did for SMA image, because Orochi is located 10 arcsec away from phase center on CARMA image. The corrected flux densities of the extended component and the unresolved component are 10.5 ± 4.3 mJy and 14.1 ± 3.1 mJy, respectively. The estimated source size of the extended component by SMA and CARMA is also listed in Table 7. We suggest that the SMA and CARMA source sizes are consistent if we consider the uncertainties of the measured sizes.

The discovery of the extended submm/mm bright component is distinguishing from almost all previously studied SMGs. For instance, the median source size moderately bright SMGs (with a typical flux of ~ 2 mJy at 1300 μm or ~ 7 mJy at 850 μm) was measured to be $\sim 0''.4$; no source larger than $1''.2$ has been reported (Tacconi et al. 2006). High-resolution radio observations are used to derive the median source size of $0''.65$ in SCUBA SMGs in the Lockman Hole (Biggs & Ivison 2008). Recently, brighter SMGs, AzTEC1 (15 mJy in 890 μm) and GN20 (27 mJy; Iono et al. 2006a), have also been observed with SMA; their source sizes were estimated as approximately $0''.3$ and $0''.6$, respectively (Younger et al. 2007); these values are similar to those of fainter SMGs. However, extended submm/mm structure at high redshift is observed in HzRGs such as B3 J2330+3927 (De Breuck et al. 2003) and 4C 60.07 (Ivison et al. 2008). A lensed SMG, SMM J02399-0136, is known to have an extended mm bright structure, and its corrected source size is $\sim 5''$. (Ivison et al. 2010c).

It should be noted that uv data suggesting the presence of extended emission can also be fitted with a model with multiple sources. For instance, AzTEC11, another bright SMG, can be modeled by two compact components with a separation of $\sim 2''$ (Younger et al. 2009). However, in the case of Orochi, we found no multiple compact components in the VLA image with the beam size of $1''.3$. Therefore, Orochi has certainly an extended component, although the size has not been precisely determined yet.

5.2 SED and redshift of Orochi

We conducted SED fitting and estimated the photometric redshift of Orochi using two methods. One involves the fitting of an SED to the optical and NIR data, and the other involves the use of submm/mm and radio data. The former corresponds to flux from stellar emission, and the latter, to cold dust emission.

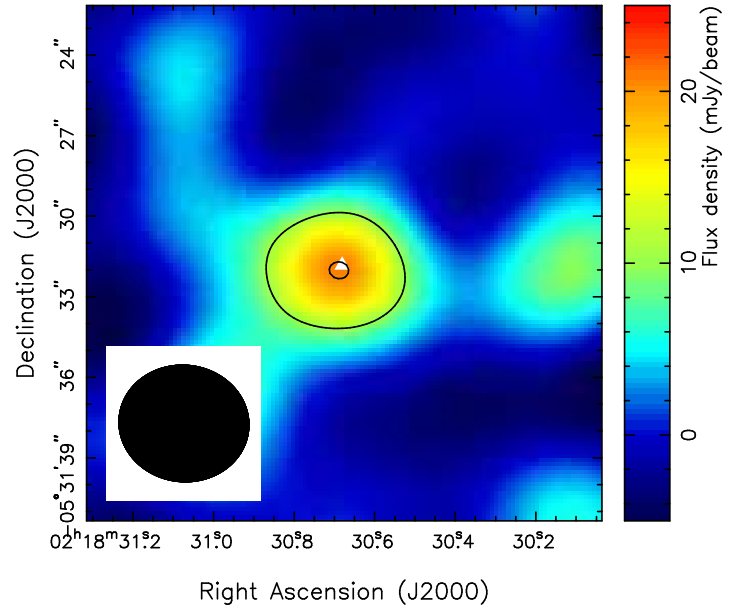


Figure 8. The SMA 880 μm image of the extended component of Orochi, produced by the residual visibility data after subtracting unresolved component in the uv domain (See section 5.1). The contour levels are 2.5 , and 5σ ($1 \sigma = 4.1$ mJy). The synthesized beam is shown on the lower left. The white triangle marks the position of the compact component.

Table 7. Summary of submillimeter/millimeter bright components.

	Size	Flux density
SMA 880 μm		
compact	unresolved	48.6 ± 4.0 mJy
extended	$4''.0 \pm 1''.2$	42.1 ± 20.3 mJy
CARMA 1300 μm		
compact	unresolved	14.1 ± 3.1 mJy
extended	$2''.7 \pm 1''.2$	10.5 ± 4.3 mJy

5.2.1 Optical and NIR photometric redshift

The optical/NIR photometric redshift is calculated using the code *Hyperz* (Bolzonella et al. 2008), with u_R , B , V , Rc , i' , z' , J , and K . The default SED template of Coleman et al. (1980), extended using the Bruzual & Charlot (1993) model, is adopted. The obtained redshift is 1.39 ($\chi^2 = 4.7$), with the 68% confidence interval of $1.383 - 1.402$.

Next, by fixing the redshift to $z = 1.39$, we carried out SED fitting using the *GALAXEV* model (Bruzual & Charlot 2003) to obtain its physical properties of the galaxy. Two star formation histories of instantaneous burst and continuous burst models are adopted, with the Salpeter initial mass function and the Calzetti (2000) dust extinction curve. The results are shown in Fig. 9; it can be observed that the optical/NIR SED is well fitted by the

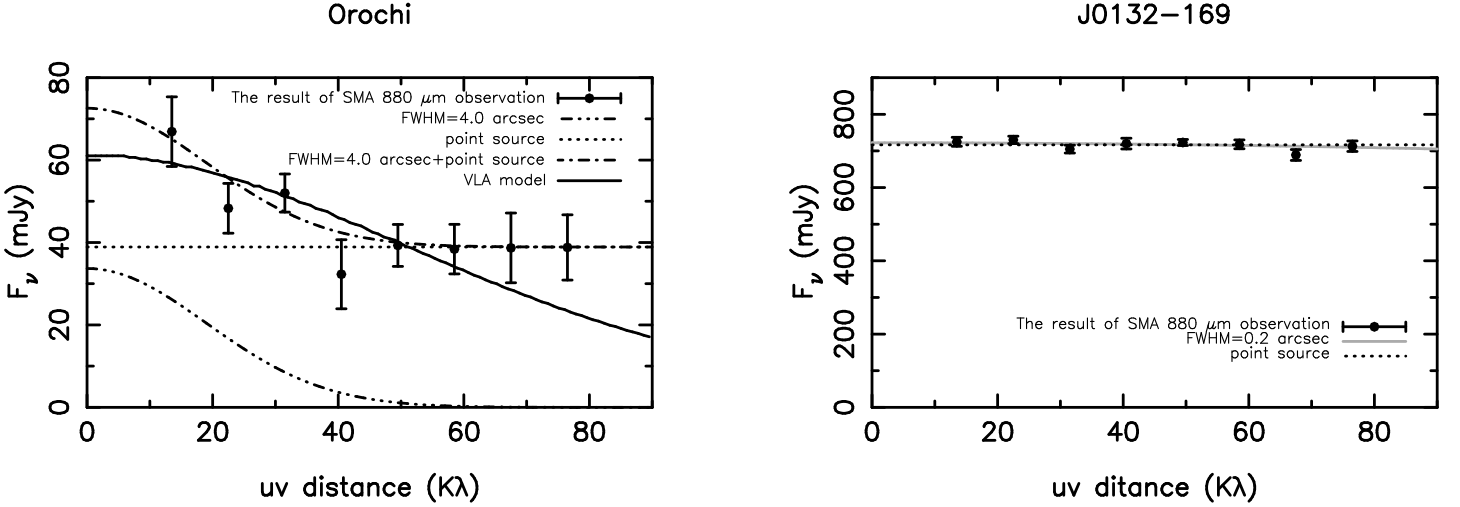


Figure 6. 880 μm visibility amplitude as a function of the baseline lengths (uv distances) toward Orochi (left) and the visibility calibrator (right), along with the results of Gaussian and point source fitting. These plots only show the real part of the visibilities, and the flux densities are not primary-beam corrected on these plots. The visibility amplitude of the calibrator (right) is well modeled with an unresolved point source, whereas Orochi can be fitted with two components, i.e., a combination of a Gaussian shaped component with a FWHM of $\sim 4''$ (dash-dot-dot-dotted line) and an unresolved point source (dotted line). The resultant fitting is indicated by a dot-dashed line. The solid curve line shows the amplitude function derived from the VLA source size ($1''.84 \times 0''.95$ at PA 23.9°), and its amplitude is scaled to be fitted to the SMA result.

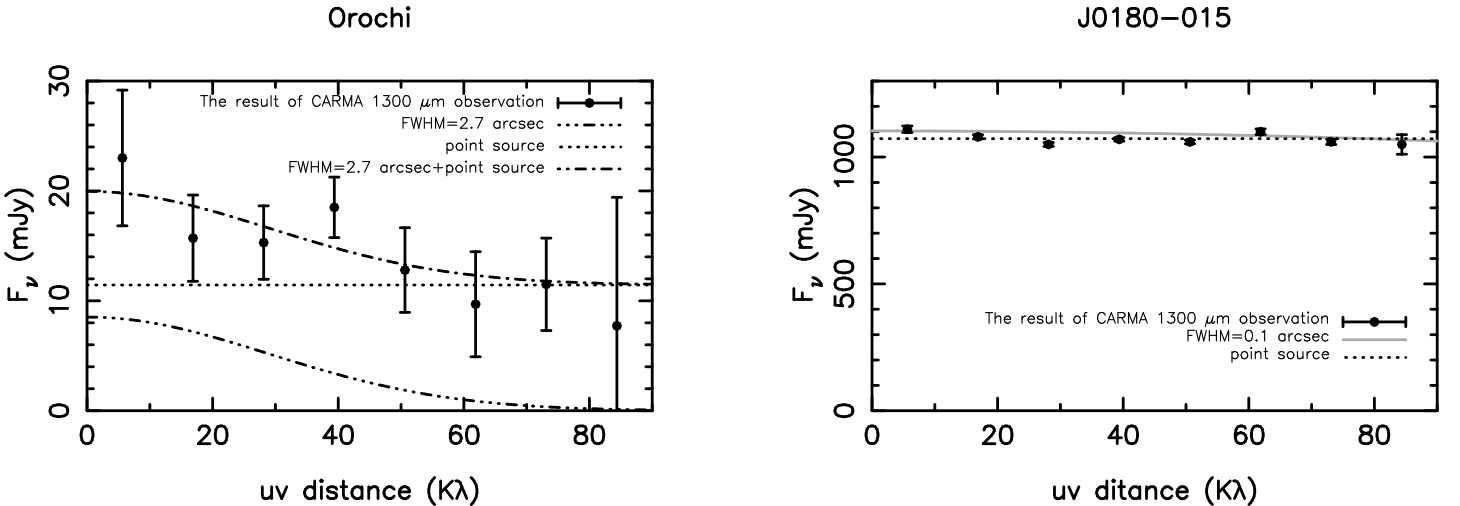


Figure 7. 1300 μm visibility amplitude as a function of the baseline lengths (uv distances) toward Orochi (left) and the visibility calibrator (right), along with the results of Gaussian and point source fitting. These plots only show the real part of the visibilities, and the flux densities are not primary-beam corrected on these plots. The visibility amplitude of the calibrator (right) is well modeled with an unresolved point source, whereas Orochi can be fitted with two components, i.e., a combination of a Gaussian shaped component with a FWHM of $\sim 2''.7$ (dash-dot-dot-dotted line) and an unresolved point source (dotted line). The resultant fitting is indicated by a dot-dashed line.

500 Myr instantaneous burst model, with a stellar mass of $1.8 \times 10^{11} M_\odot$ and a dust extinction of $E(B-V) = 0.31$.

5.2.2 submm/mm and radio photometric redshift

We used a Monte Carlo photometric redshift method (Hughes et al. 2002; Aretxaga et al. 2003) to estimate the photometric redshift based on submm/mm and radio data.

A Monte Carlo photometric redshift method has been developed to take into account constraining prior information such as a range of local SED templates, the

favoured evolving luminosity function of dust enshrouded star-forming galaxies to $z \approx 2$, and the amplification of certain fields. We assume that the SEDs of SMGs are well represented by 20 SEDs of local starbursts, ULIRGs, and AGN to provide FIR–radio SEDs. These SEDs cover a wide range of FIR luminosities ($10^{9.0} - 10^{12.3} L_\odot$) and temperatures (25–65 K). See details in Aretxaga et al. (2007) for the method. We adopt a very conservative estimate for the amplification of the source ($\mu = 10$).

We used the FIR to radio portion of the SED, i.e., the photometric data at 160 μm (Spitzer; upper limit), 1000

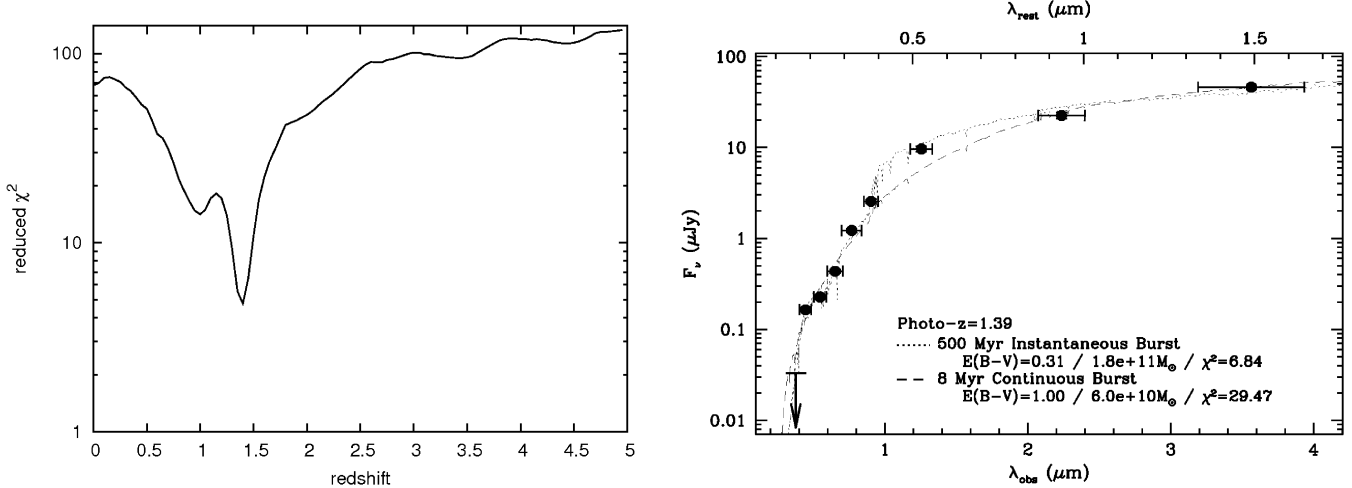


Figure 9. Result of Optical/NIR photometric redshift and SED fitting of Orochi. Left panel shows the reduced χ^2 versus photometric redshift obtained by Hyperz code. Right panel shows the best-fit optical/NIR synthetic model spectra, by fixing the redshift to 1.39 obtained by Hyperz. The dotted and dashed lines show the resultant spectra assuming instantaneous and continuous starburst, respectively.

μm (Z-Spec), 1100 μm (AzTEC/ASTE), 1500 μm (Z-Spec), 20 cm (VLA) and 50 cm (GMRT), for the derivation of the photometric redshift. These three photometric data at submm/mm wavelength were selected as representatives of the Rayleigh-Jeans slope.

The derived redshift probability distribution is shown in Fig. 9. The estimated redshift is $3.4^{+0.7}_{-0.5}$. The peak of the probability density distribution is very stable to changes in magnification. Solution were derived FIR amplification factors ranging from 1 (no magnification) to 50, finding peak values between 3.3 and 3.5. As the magnification increases, we find a slight transfer of the probability density towards higher redshift values, which displaces the 68 percent confidence interval up to $3.4^{+0.7}_{-0.5}$.

5.2.3 $z \sim 1.4$ or ~ 3.4 ?

We now discuss the inconsistency between the two photometric redshift results. The optical/NIR photometric redshift suggests $z \sim 1.4$, while the submm/mm and radio photometric redshift suggests $z \sim 3.4$. Next, we show that this apparent discrepancy can be understood by observing an optically dark SMG lying at $z \sim 3.4$ behind a foreground galaxy located around $z \sim 1.4$, visible at optical/NIR wavelengths.

The optical/NIR-based photometric redshift of ~ 1.4 seems to be robust because we obtain nearly continuous detections in optical/NIR, i.e., ~ 0.4 μm–2.2 μm; its SED shows a clear break feature at around 1.2 μm, which is very likely to be a 4000 Å break around $z \sim 1.4$. Although the IRAC colours of Orochi, $\log(S_{5.8\mu\text{m}}/S_{3.6\mu\text{m}}) = 0.21$ and $\log(S_{8.0\mu\text{m}}/S_{4.5\mu\text{m}}) = 0.28$, suggest the existence of an obscured AGN (Lacy et al. 2004), such a sharp 4000 Å break can be reproduced solely by stellar spectra, (i.e., it is very difficult to produce a clear break with AGN models). Therefore, we suggest that the observed optical/NIR spectrum is dominated by a stellar component; Further, the possible 4000 Å break feature reliably constrains the redshift. The

resultant reduced χ^2 distribution shows a sharp peak at $z \sim 1.4$.

On the other hand, the submm/mm and radio photometric redshift is also fairly well constrained with almost continuous coverage from 880 μm to 1500 μm combined with radio and MIPS upper limits. Although it is possible to fit the observed SED with an SMG at $z = 1.4$, it requires an SED template with a very low dust temperature, $T_{\text{dust}} \sim 20$ K, which is nearly the lowest measured dust temperature distribution among SMGs (e.g., Kovács et al. 2006). Refer to the next section for a detailed discussion of SED modeling with a grey-body.

Another constraint on the redshift of the gas/dust component comes from Z-Spec observations. In general, the line-to-continuum ration (L/C ratios) are expected to be smaller for higher J transitions because the continuum flux increases with ν^{3-4} . On the other hand, the CO line flux increases with J^2 or ν^2 for thermalized conditions, and since high-J lines are often subthermally excited, they are much weaker than in a thermalized case.

As no emission line features are detected for the intense continuum emission, the upper limit on the L/C ratio is 0.1–0.3 (2 σ) accross the Z-Spec band. This value is low if we assume a redshift of ~ 1.4 , where CO($J=4-3$), CO($J=5-4$), and CO($J=6-5$) wshould be expected to be in the Z-Spec band.

We collected the L/C ratios from the measured CO fluxes and adjacent continuum emission using interferometers in the literature and we found that L/C ratios are typically in the range of 3–20 for high-z quasars (Downes et al. 1999; Weiß et al. 2007; Omont et al. 1996; Bradford et al. 2009; Wang et al. 2010), radio galaxies (Papadopoulos et al. 2000), SMGs (Greve et al. 2005; Tacconi et al. 2006)³, and

³ There are no direct descriptions of the continuum fluxes, and L/C ratios are estimated from the CO($J=4-3$) spectrum in these papers.

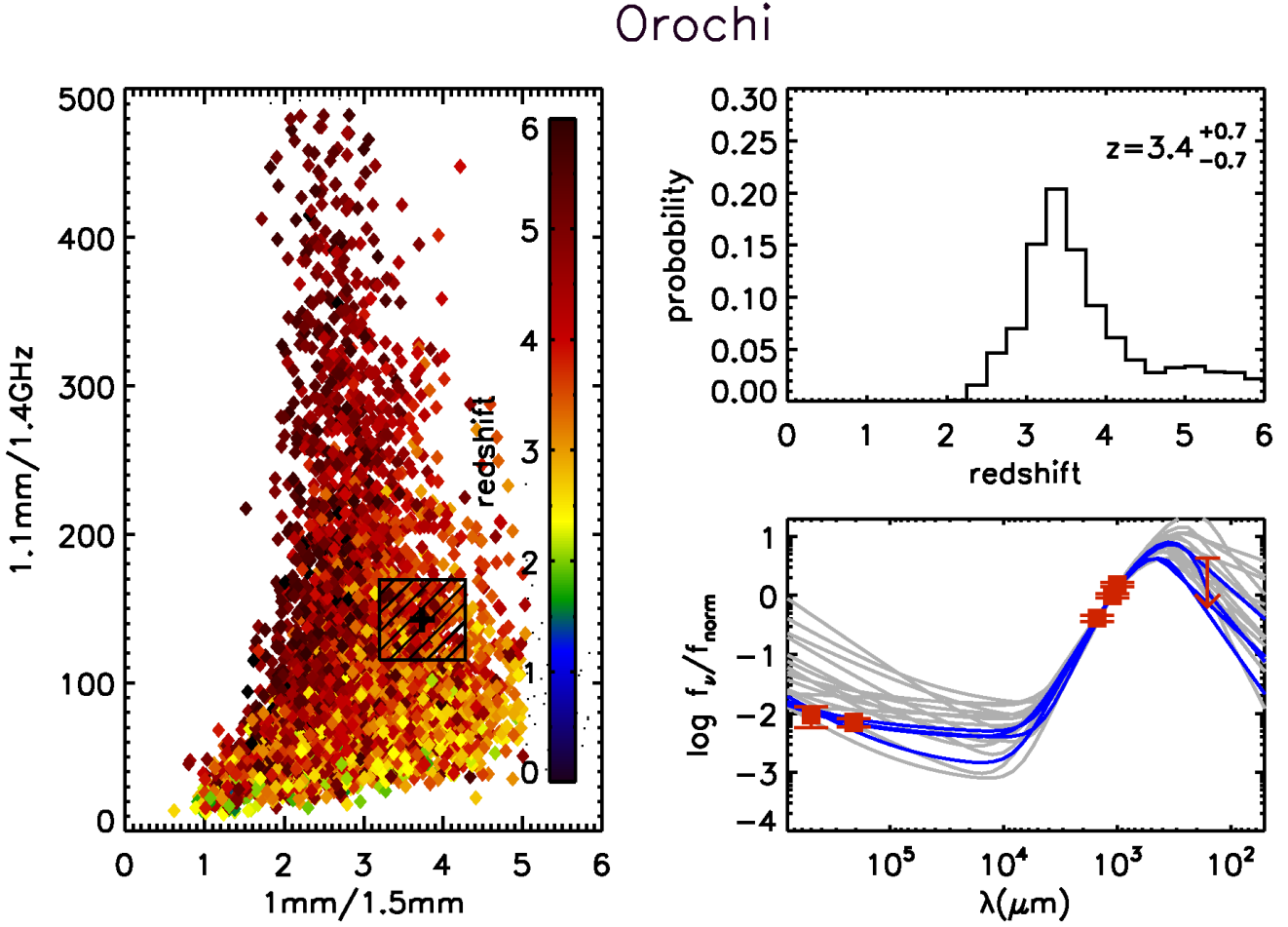


Figure 10. The left panel shows the colour-colour-redshift plot for Orochi. The flux ratios of the mock galaxies are represented as diamonds, and their redshifts are colour-coded according to the scale shown in the panel on the right. The cross represents the measured colours of Orochi, and the dashed box shows the 1σ uncertainty in each colour. The top right panel shows estimated redshift probability distribution of Orochi. In the bottom right panel, the observed SED of Orochi normalised to the flux densities at $1000\text{ }\mu\text{m}$ is shown as squares and arrows. The arrow indicates 3σ upper limits. The squares denote the detection at a level $\geq 3\sigma$, with 1σ error bars. The template SEDs (lines) are redshifted to $z = 3.4$. The template SEDs at this redshift compatible within 3σ error bars with the SED of Orochi are displayed as blue lines. The photometric data are shown at $1000, 1100, 1500\text{ }\mu\text{m}, 20$ and 50 cm , and The upper limit is shown at $160\text{ }\mu\text{m}$.

a local ULIRG (Matsushita et al. 2009). This indicates that we have already achieved sufficient line sensitivity for the observed continuum flux level if Orochi is lying at around $z \sim 1.4$.

On the other hand, the observed low L/C ratio is acceptable if Orochi is at $z \sim 3.4$; this is because the observed J lines such as CO($J=9-8$) to CO($J=13-12$) in the Z-Spec band are considered to be of a much higher order. Smaller L/C ratios around unity have been reported for CO($J=9-8$) in APM J08279+5255 (Downes et al. 1999; Weiß et al. 2007) and the Cloverleaf (Bradford et al. 2009). It should be emphasized that these two quasars show exceptionally highly excited CO lines up to CO($J=10-9$) level (Weiß et al. 2007); the measured CO SED suggests that the CO fluxes are consistent with the thermalized condition as they are expected to increase with ν^2 up to $J \sim 10$. Other typical high- z quasars as well as starburst cores of local IR bright galaxies

like M82 and NGC 253 become subthermal at around $J \sim 4 - 6$; a simple LVG model calculation suggests that the expected CO($J=9-8$) flux in a typical starburst core (e.g., gas density $n_{\text{H}_2} = 10^4\text{ cm}^{-3}$ and kinetic temperature $T_{\text{kin}} = 60\text{ K}$) will be smaller than the thermalized-case flux by a factor of 20 or more; i.e., it is natural to expect that the L/C ratio for these high- J lines are much smaller than unity, as observed in Orochi with Z-Spec.

Here, we briefly comment on the constraint on redshift from [CII] emission ($\nu_{\text{rest}} = 1.9019\text{ THz}$); this line can be in the Z-Spec band if $5.2 < z < 9.5$. The upper limit to the [CII] line luminosity is $L_{[\text{CII}]} < 3.6 \times 10^9 L_\odot$ (2σ), if it is at $z = 5.5$ with a line width of 780 km s^{-1} , which is a median value for SMGs (e.g., Greve et al. 2005). This results in a strict upper limit on the [CII] to FIR luminosity ratio, $L_{[\text{CII}]} / L_{\text{FIR}} < 3.6 \times 10^{-5}$ (2σ), which is already much smaller than the observed $L_{[\text{CII}]} / L_{\text{FIR}}$ ratios

for high- z quasars/SMGs, i.e., $\sim 10^{-4} - 10^{-3}$ (Iono et al. 2006b; Maiolino et al. 2009; Ivison et al. 2010a). We, therefore, suggest that the redshift of Orochi would be less than ~ 5 .

In summary, we suggest that the mm/submm bright component of Orochi is likely to be at $z \sim 3.4$, whereas the optical/NIR counterpart candidate with a photometric redshift of ~ 1.4 is a foreground galaxy with an old stellar population. Although it is difficult to ignore the possibility that both systems, the i.e., submm-to-radio bright component and its optical/NIR counterpart, are lying at the same redshift (i.e., at $z \sim 1.4$), this possibility requires an exceptionally low dust temperature for SMGs ($T_{\text{dust}} \sim 20$ K) as well as a low-excitation molecular gas for which the mid- J lines such as CO($J=4-3$) are not well excited.

In the following sections, we estimate physical quantities for two cases — $z \sim 3.4$ and $z \sim 1.4$ — because it is difficult to completely reject the latter possibility at this moment, even though the former seems more probable.

5.2.4 Dust SED model using a grey-body

We model SEDs from FIR to radio wavelengths using grey bodies. To draw SEDs at radio wavelengths, we assume the radio-FIR correlation (e.g., Condon 1992; Ivison et al. 2010b). This correlation is described as the q -value⁴. It is known that the mean of q_{TIR} for SMGs is 2.32 with a scatter of 0.34 (Michałowski et al. 2010). We use this typical q_{TIR} of known SMGs for extrapolating the radio spectrum. Moreover, L_{IR} is derived from the SED of a model grey-body.

We also derived the radio emissivity index α ($S \propto \nu^\alpha$) of Orochi. Orochi has two photometric data at radio wavelengths, 20 cm (VLA) and 50 cm (GMRT). From these data, the radio emissivity index α of Orochi is derived as $-0.33^{+0.29}_{-0.32}$. Comparing α of local star-forming galaxies (~ -0.7 to -0.8 ; Condon 1992), and SMGs at $z \sim 2$ (-0.75 ± 0.06 ; Ibar et al. 2010), the measured α in Orochi is found to be rather closer to a pure thermal radio spectrum. If Orochi is located at $z > 3$, the α of Orochi seems to be consistent with predictions that non-thermal radio continuum emission will be suppressed at high z ($z > 3$ or so) due to the increased energy losses from the inverse Compton scattering off in the cosmic microwave background to the cosmic ray electrons (Murphy 2009).

For the models based on the optical/NIR photometric redshift of 1.4, the dust emissivities were derived as $\beta = 1.4$, 1.5, and 1.9 for $T_{\text{dust}} = 40$, 30, and 20 K, respectively, by fitting the Z-Spec continuum data at 1000–1500 μm . We find that a low dust temperature, 20 K, is required if a photometric redshift of 1.4 is assumed. Possibilities of higher dust

⁴ The q -value is defined as $q \propto \log(L_{\text{FIR}}) - \log(I_{1.4\text{GHz}})$, where $I_{1.4\text{GHz}}$ is a rest-frame 1.4 GHz luminosity density and L_{FIR} is defined as the 42.5–122.5 μm FIR luminosity. This relation corresponds to the median q -value, $< q > \sim 2.3$, with a rms scatter of ≤ 0.2 in nearby normal galaxies (Condon 1992) and 2.34 ± 0.01 in local IRAS galaxies (Yun et al. 2001). On the other hand, we use the total 8–1000 μm IR (L_{IR}) as an indicator of dust emission. In this case, the q -value is redefined as $q_{\text{TIR}} \propto \log(L_{\text{IR}}) - \log(I_{1.4\text{GHz}})$. The value of q_{TIR} is 2.64 ± 0.02 in local galaxies, which is consistent with the above q -value (Bell 2003).

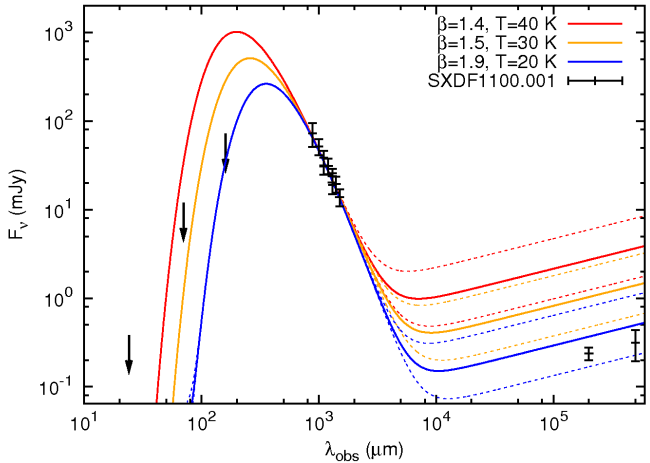


Figure 11. The SED of Orochi and SED fitting results in FIR-radio wavelengths, assuming $z=1.4$. We calculated grey-bodies for $T_{\text{dust}} = 20$, 30, and 40 K. The β for each grey-body is estimated by fitting the Z-spec continuum data at 1000–1500 μm . The dashed lines show the scatter of the q -value. The upper limits are shown at 24, 70, and 160 μm , and the photometric data are shown at 880, 1000, 1100, 1200, 1300, 1400, 1500 μm , 20 and 50 cm. We find that the dust temperature of Orochi must be as low as 20 K if we assume $z \sim 1.4$.

temperatures such as 30 K and 40 K are clearly eliminated because the upper limits at 24, 70, and 160 μm bands tight constraints on the dust temperature. The radio flux density also seems to be consistent with a model with T_{dust} of 20 K. Again, higher dust temperatures such as 30 K and 40 K are not acceptable because at such high dust temperatures, L_{IR} is overluminous in terms of radio luminosity, as clearly shown in Fig. 11.

On the other hand, for models based on the submm/mm-to-radio photometric redshift of ~ 3.4 , we find that the observed submm/mm to radio SED can be well explained by the dust temperature of ~ 30 K, as shown in Fig. 12. This is consistent with the typical dust temperature of SMGs (e.g., Kovács et al. 2006).

5.3 A possible positional offset between a submm-radio bright component and an optical/NIR counterpart candidate

Here, we present a detailed comparison of the multi-wavelength images of Orochi. Fig. 13 displays the peak positions of CARMA, SMA, and VLA sources listed in Table 3 superposed on the Subaru z' -band image. We find a possible positional offset between the optical peak and the submm/mm/radio peaks; its separation is approximately $0''.1$ – $0''.7$. Although these separations are smaller than the beam sizes of the observations, the evaluated combined-astrometry errors listed in Table 3 are smaller than the claimed offset, especially in declination. Furthermore, all three observations (i.e., CARMA, SMA, and VLA) show a similar tendency, i.e., the peaks of these wavelengths are located at the north west part with respect to the z' -band peak, which is also associated with the K band peak. These facts suggest the possible existence of a spa-

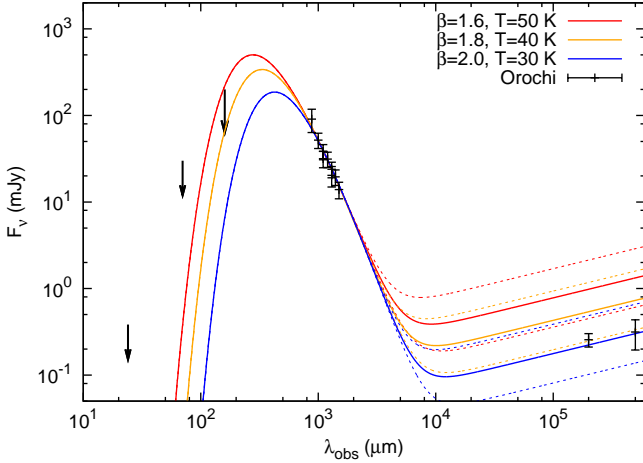


Figure 12. The SED of Orochi and SED fitting results in FIR-radio wavelengths, assuming $z=3.4$. We calculated grey-bodies for $T_{dust} = 30, 40$, and 50 K. The β for each grey-body is estimated by fitting the Z-spec continuum data at $1000\text{--}1500 \mu\text{m}$. The dashed lines show the scatter of the q -value. The upper limits are shown at $24, 70$, and $160 \mu\text{m}$, and the photometric data are shown at $880, 1000, 1100, 1200, 1300, 1400, 1500 \mu\text{m}$, 20 and 50 cm . We find that the dust temperature of Orochi seems to be as low as 30 K if we assume $z \sim 3.4$.

tial offset between the peaks in the optical/NIR and the submm/mm/radio wavelengths.

As discussed in section 5.2.3, the optical/NIR bright counterpart candidate can be a foreground source of Orochi. In this case, the extended bright structure observed in the optical and NIR bands, i.e., the north-west extension from the optical/NIR peak positions around the SMA, CARMA, and VLA is probably a true optical counterpart of Orochi and is blended with the foreground source.

In order to confirm this possibility, we need higher angular resolution images for all wavelengths. Future ALMA observations combined with HST or ground-based AO observations will be conducted for addressing this issue.

5.4 The Origin of $1100 \mu\text{m}$ Flux in Orochi

The observed $880 \mu\text{m}$ flux of Orochi, $\sim 91 \text{ mJy}$, makes this one of the brightest SMGs known to date. For instance, it is much brighter than the brightest SMGs revealed by SHADES ($\sim 10\text{--}15 \text{ mJy}$ at $850 \mu\text{m}$; Coppin et al. 2006) and brighter or comparable to the known lensed submillimeter bright high- z sources such as the Cloverleaf ($58.8 \pm 8.1 \text{ mJy}$ at $850 \mu\text{m}$, with a lens magnification of 11; Barvainis et al. 2002; Venturini et al. 2003), APM08279+5225 ($84 \pm 3 \text{ mJy}$ at $850 \mu\text{m}$, with a lens magnification of 7; Barvainis et al. 2002; Lewis et al. 2002) and SMMJ2135-0102 ($106.0 \pm 7.0 \text{ mJy}$ at $870 \mu\text{m}$, with a lens magnification of 32; Swinbank et al. 2010). A similar bright SMG has also been uncovered by MAMBO on IRAM 30 m observations ($30 \pm 2 \text{ mJy}$ at $1200 \mu\text{m}$; Lestrade et al. 2010). SPT surveys detected 47 dust-dominated mm sources above 10 mJy at 1.4 mm in 87 deg^2 , and 20 of 47 do not have counterparts at low- z universe (Vieira et al. 2010). If all of 20 are indeed SMGs located at high- z universe, a surface density of

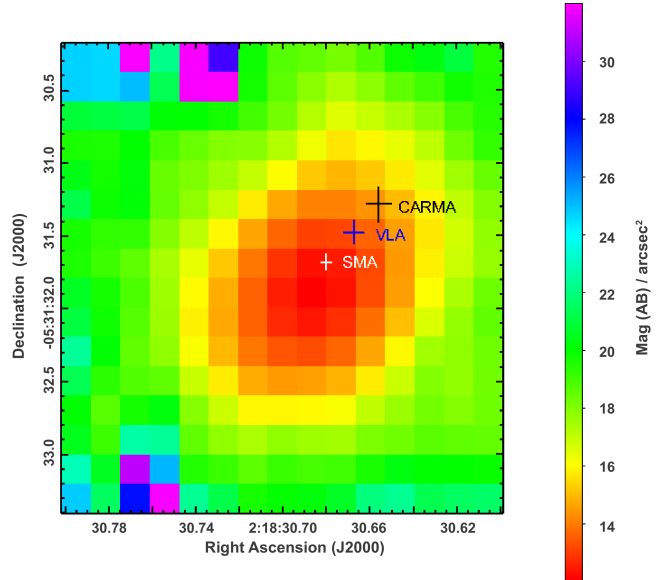


Figure 13. Radio/mm/submm peak positions superposed on the z' -image of Orochi. The white, black, and blue crosses (expressing the position uncertainties) correspond to the SMA, CARMA, VLA peak positions, respectively. The unit of the background z' -band image is Mag (AB) per arcsec^2 .

these ultra-bright SMGs is ~ 0.23 sources per 1 deg^2 . Considering we found only 1 ultra-bright SMG in about 0.33 deg^2 , which is surveyed area in SXDF, it is consistent that Orochi belongs to the same population with SPT sources.

It is possible that Orochi is gravitationally lensed, because many of the ultra-bright SMGs are often strongly amplified by a foreground massive cluster of galaxies (e.g., Wilson et al. 2008b; Johansson et al. 2010; Swinbank et al. 2010; Ivison et al. 2010a). The recent model analysis for submm/mm count shows that these ultra bright SMGs are likely to be gravitationally lensed by foreground massive halos (Lima et al. 2010; Hezaveh & Holder 2010). Although we found no catalogued foreground clusters around Orochi, analysis of photometric redshifts of optically visible objects around Orochi suggest that there are cluster candidates at $z \sim 0.4$ and 1.4 , and they may be partially responsible for lensing.

It is also possible that this SMG is gravitationally lensed by other foreground galaxies near Orochi. Theoretically, when a galaxy causes a lensing effect on another galaxy, the former galaxy is located at around less than 1 arcsec from the latter. In the case of Orochi, the optical/NIR bright foreground galaxy at $z \sim 1.4$ can be a candidate for the lensing galaxy. The estimated stellar mass of the optical/NIR bright source by SED fitting is $\sim 10^{11} M_\odot$; therefore, it is sufficiently massive to cause gravitational lensing. In fact, some of $500 \mu\text{m}$ -selected ultra bright SMGs are indeed gravitationally lensed by foreground galaxies (Negrello et al. 2010).

Nevertheless, we note that there is no clear evidence for strong lensing in existing high-resolution optical/infrared images, for instance, the presence of multiple and/or distorted structures. This situation is different from that of SMM J2135-0102, another ultra-bright SMG, where distorted/elongated images can be clearly observed even in the

resolution of the IRAC bands, although the noise level of the IRAC bands in SXDF is at least 10 times better than that of SMM J2135-0102 (Swinbank et al. 2010).

On the other hand, the situation of Orochi is similar to that of HDF850.1 (7.0 ± 0.4 mJy at $850 \mu\text{m}$; Hughes et al. 1998). The photometric redshift of HDF850.1 is $z = 4.1^{+0.6}_{-0.5}$ (Cowie et al. 2009) and it is indicated that HDF850.1 is gravitationally lensed by an elliptical galaxy at $z = 1.22$ about 1 arcsec away from HDF850.1 (Hughes et al. 1998; Dunlop et al. 2004; Cowie et al. 2009). HDF850.1 also has no clear counterpart image in the mid- and near-infrared deep images.

The elevated mm/submm fluxes can be from non-thermal synchrotron emission if they are powered by a radio-loud AGN. In fact, wide-field mm surveys often uncover such non-thermal sources (e.g., Voss et al. 2006; Vieira et al. 2010). In the case of Orochi, however, we conclude that the submillimeter flux is dominated by thermal dust emission heated by massive stars and not by a radio-loud AGN because the submm-to-radio SED can be well reproduced by the known L_{IR} -to-radio correlation observed in previously studied SMGs and local starburst galaxies, as shown in section 5.2.4. Absence of the time variability in the submm/mm fluxes of Orochi, i.e., in the $1100 \mu\text{m}$ flux measured by AzTEC in November/December 2008, the $1300 \mu\text{m}$ flux by CARMA in August 2009, the $880 \mu\text{m}$ flux by SMA in December 2009, and the Z-Spec data in November 2009, may also suggest the thermal origin of the elevated flux of Orochi.

5.5 Estimation of physical properties of Orochi

We estimate the physical quantities of Orochi, i.e., L_{IR} , dust mass (M_d) and gas mass (M_{gas}), by adopting two possible redshifts and models in section 5.2: (1) $z = 1.4$, for which the SED model of the grey-body with $T_d = 20 \text{ K}$ and $\beta = 1.9$, and (2) $z = 3.4$, for which we used an averaged SED template of the 4 best fitted SEDs (the SED templates of NGC3227, NGC7771, IRAS05189-2524, and IRAS12112+0305), providing $T_d = 35 \text{ K}$ and $\beta = 2.0$. Here, we simply show the physical quantities of Orochi using the apparent luminosity, i.e., $L_{\text{IR}} = \mu L_{\text{IR}}^*$, where L_{IR}^* is the intrinsic luminosity and μ is the magnification factor, because we have no constraint on the magnification factor (if any) at this moment. Furthermore, here, we do not distinguish between the compact and extended components.

We estimated SFR using the equation below.

$$\text{SFR}(\text{M}_\odot \text{yr}^{-1}) = 4.5 \times 10^{-44} L_{\text{IR}}(\text{ergs s}^{-1}) \quad (2)$$

(Kennicutt. 1998). M_d is derived as

$$M_d = \frac{S_{\text{obs}} D_L^2}{(1+z) \kappa_d(\nu_{\text{rest}}) B(\nu_{\text{rest}}, T_{\text{dust}})}, \quad (3)$$

where S_{obs} is the observed flux density. In this paper, the flux density is at $1100 \mu\text{m}$, ν_{rest} is the rest-frame frequency; $\kappa_d(\nu_{\text{rest}})$, the dust mass absorption coefficient; and $B(\nu_{\text{rest}}, T_{\text{dust}})$, the Planck function (Hughes et al. 1997). We assume that the absorption coefficient varies as $\kappa_d \propto \nu^\beta$. We adopt $\kappa_d(125 \mu\text{m}) = 2.64 \pm 0.29 \text{ m}^2 \text{kg}^{-1}$, the average value of various studies (Dunne et al. 2003). The gas mass is then derived using a gas-to-dust mass ratio of 54, which is an average value for SMGs in Kovács et al. (2006).

The derived quantities are listed in Table 8, along with

the gas consumption time scale, which is defined as the ratio of $M_{\text{gas}}/\text{SFR}$ or $1/\text{SEF}$, where SEF refers to the star formation efficiency. However it should be noted that many of these results are rough estimates based on median relations, assumption about the SED.

Table 8 shows that if $z \sim 3.4$, Orochi will consume its gas reservoir within a short time scale ($\sim 3 \times 10^7 \text{ yr}$), which is indeed comparable to those in extreme starbursts like the hearts of local ULIRGs (e.g., Kennicutt. 1998). On the other hand, if this source has a lower z of ~ 1.4 , Orochi has a fairly long gas consumption time scale of $\sim 1 \times 10^9 \text{ yr}$, which is almost comparable to that of star-forming clouds in the disks of spiral galaxies in the local universe, and hence, rather unlikely.

5.6 Starburst form of Orochi

One of the remaining key questions of Orochi is its form of starbursts: What type of star formation or starburst produces such an SFR elevated to $\sim 870 M_\odot \text{ yr}^{-1}$ (if $z \sim 1.4$) or $11000 M_\odot \text{ yr}^{-1}$ (if $z \sim 3.4$)? Recent high angular resolution studies of high-z quasars and SMGs suggest that Eddington-limited maximal starbursts often occur at the heart of these extreme objects (Younger et al. 2008; Riechers et al. 2009). In these galaxies, the peak SFR and L_{IR} surface densities reach up to $\Sigma_{\text{SFR}} \sim 10^3 M_\odot \text{ yr}^{-1} \text{ kpc}^{-2}$ and $\Sigma_{L_{\text{IR}}} \sim 10^{13} L_\odot \text{ kpc}^{-2}$, respectively; these values are close to the theoretical maximum value imposed by the Eddington limit (Elmegreen et al. 1999; Thompson et al. 2005). Therefore, it is intriguing to address whether the $\text{SFR}/L_{\text{FIR}}$ surface densities at the center of Orochi are close to the maximum starburst condition or not.

We estimate the surface gas mass density (Σ_{gas}), SFR surface density (Σ_{SFR}) and L_{IR} surface density ($\Sigma_{L_{\text{IR}}}$) for these two components (Table 7), respectively.

We assume that the source size of the unresolved compact component is $0''.4$, which is the median size of the submillimeter bright region of SMGs (Chapman et al. 2004; Tacconi et al. 2006). The derived surface densities for two possible photometric redshifts, ~ 1.4 and ~ 3.4 , are listed in Table 9.

The Σ_{gas} and other derived densities of the extend component are similar to or higher than those of the star-forming disk regions in local spiral galaxies (e.g., Nishiyama et al. 2001; Wong & Blitz et al. 2002).

This indicates that the extended component of Orochi is a large lump of relatively moderate starburst regions, although we should note that the extended structures can be a lensed image. We then need to estimate the magnification factor to discuss the quantitative properties of star formation.

On the other hand, the derived parameters of the compact component are rather close to those of ULIRGs in the local universe, i.e., the predicted maximum limit (e.g., Riechers et al. 2009), although it still depends on the assumed source size and magnification factor (if any).

SUMMARY

An ultra-bright SMG, Orochi, has been detected using with the AzTEC on ASTE. Subsequent CARMA, SMA, and Z-

Table 8. Estimated IR luminosity, dust mass, gas mass, star formation rate, and inverse of star formation efficiency (corresponding to a gas consumption time scale) for two possible redshifts, $z = 1.4$ (model 1) and 3.4 (model 2), which are estimated in section 5.2.4. Here, we describe the observed quantities as μL_{IR}^* , μM_{d}^* , μM_{gas}^* , and μSFR^* , where μ indicates the magnification factor. Note that $1/\text{SFE}$ is independent of magnification.

model	z	T_d	β	μL_{IR}^*	μM_{d}^*	μM_{gas}^*	μSFR^*	$1/\text{SFE}$
(1)	1.4	20 K	1.9	$5.1 \times 10^{12} L_{\odot}$	$1.7 \times 10^{10} M_{\odot}$	$9.1 \times 10^{11} M_{\odot}$	$870 M_{\odot}\text{yr}^{-1}$	$1.0 \times 10^9 \text{ yr}$
(2)	3.4	35 K	2.0	$6.3 \times 10^{13} L_{\odot}$	$5.8 \times 10^9 M_{\odot}$	$3.1 \times 10^{11} M_{\odot}$	$11000 M_{\odot}\text{yr}^{-1}$	$2.8 \times 10^7 \text{ yr}$

Table 9. Estimated surface density of molecular gas mass, SFR, and L_{IR} (Σ_{gas} , Σ_{SFR} , and $\Sigma_{L_{\text{IR}}}$, respectively) for two components revealed by SMA, i.e., spatially unresolved, compact component (the size was assumed to be $0''.4$) and spacially extended component ($4''.0$). We adopted a scale of 8.432 kpc/arcsec for $z = 1.4$ and 7.396 kpc/arcsec for $z = 3.4$. Adopted SED models, dust temperatures, and parameters are the same as Table 8.

Model	z	T_{dust}	Component	Size	Σ_{gas}	Σ_{SFR}	$\Sigma_{L_{\text{IR}}}$
(1)	1.4	20 K	compact	$0''.4$ (3.4 kpc)	$5.4 \times 10^{10} M_{\odot}\text{kpc}^{-2}$	$5.2 \times 10^1 M_{\odot}\text{yr}^{-1}\text{kpc}^{-2}$	$3.0 \times 10^{11} L_{\odot}\text{kpc}^{-2}$
			extended	$4''.0$ (33.7 kpc)	$4.1 \times 10^8 M_{\odot}\text{kpc}^{-2}$	$3.9 \times 10^{-1} M_{\odot}\text{yr}^{-1}\text{kpc}^{-2}$	$2.3 \times 10^9 L_{\odot}\text{kpc}^{-2}$
(2)	3.4	35 K	compact	$0''.4$ (3.0 kpc)	$2.4 \times 10^{10} M_{\odot}\text{kpc}^{-2}$	$8.3 \times 10^2 M_{\odot}\text{yr}^{-1}\text{kpc}^{-2}$	$4.8 \times 10^{12} L_{\odot}\text{kpc}^{-2}$
			extended	$4''.0$ (29.6 kpc)	$6.7 \times 10^7 M_{\odot}\text{kpc}^{-2}$	$7.4 \times 10^0 M_{\odot}\text{yr}^{-1}\text{kpc}^{-2}$	$4.3 \times 10^{10} L_{\odot}\text{kpc}^{-2}$

Spec observations confirm the AzTEC/ASTE detection of Orochi. The major findings and conclusions are summarized as follows.

(i) We discovered a 37.27 ± 0.65 mJy source at $\lambda = 1100 \mu\text{m}$ in SXDF using AzTEC mounted on ASTE.

(ii) CARMA $\lambda = 1300 \mu\text{m}$ and SMA $\lambda = 880 \mu\text{m}$ observations successfully confirmed the AzTEC/ASTE detection of Orochi. The peak positions of the CARMA/SMA sources coincide with the AzTEC/ASTE peak position. In addition, these flux densities from 1300 to $880 \mu\text{m}$ are consistent with a single SED for $\beta = 1 \sim 2$. The $880 \mu\text{m}$ flux density of Orochi is ~ 91 mJy, which makes it one of the brightest SMGs after SMMJ2135-0102 (~ 106 mJy at $870 \mu\text{m}$).

(iii) The CSO 10 m telescope equipped with Z-Spec was used to conduct a blind search for redshifted molecular/atomic lines and continuum emission in the 190–308 GHz band. The measured continuum flux is consistent to the SMA/AzTEC/CARMA measurements, although no significant emission/absorption line features were found. The derived upper limit to the line-to-continuum flux ratio (L/C ratio) was 0.1–0.3 (2 σ) across the Z-Spec band.

(iv) We find that Orochi is spatially resolved and has two components, i.e., an extended structure (FWHM of $\sim 4''$) and a compact unresolved one, based on the analysis of the visibility amplitude as a function of the projected baseline length in both SMA and CARMA data. Approximately half of the total millimeter/submillimeter flux arises from the extended component. The discovery of the extended submm/mm bright component is distinguishing because such an extended bright structure has not been observed in previously studied normal SMGs, which show a median source size of $0''.4$.

(v) Multi-wavelength counterparts of Orochi have been identified near the peak position of CARMA/SMA using

optical (Subaru), NIR (UKIRT; Spitzer), MIR(Spitzer) and radio (VLA and GMRT) images.

(vi) A robust photometric redshift of 1.4 was derived using optical/NIR data and the code *Hyperz* based on a detection of possible 4000 Å break feature. On the other hand, a photometric redshift using submm/mm and radio data suggests $z \sim 3.4$, eliminating the possibility of $z < 3$. A fairly low dust temperature, $T_{\text{dust}} \sim 20 \text{ K}$, is required if $z = 1.4$, whereas T_{dust} of 30–50 K, typical for SMGs, can explain the observed FIR to radio SED for a redshift range of 3–5.

(vii) The discrepancy in photometric redshifts can be understood for an optically dark SMG lying at $z \sim 3.4$ with a foreground galaxy around $z \sim 1.4$. Indeed, we find a positional offset of $\sim 0''.2$ – $0''.7$ between sub/mm/radio peaks and optical peak, implying a possible coincidental overlap of two objects along the line of sight.

(viii) If Orochi is located at $z \sim 3.4$, higher order J -lines such as CO($J = 9 - 8$) to CO($J = 13 - 12$) fall into Z-Spec band. However we did not achieve any significant detection of lines. The upper limit on L/C ~ 0.1 – 0.3 in Z-Spec band is expected for these very high J lines.

(ix) If the millimeter/submillimeter bright component of Orochi is indeed lying at $z \sim 3.4$, the deduced apparent FIR luminosity (L_{IR}) and star formation rate (SFR) are $L_{\text{IR}} \sim 6 \times 10^{13} L_{\odot}$ and $\text{SFR} \sim 11000 M_{\odot}\text{yr}^{-1}$, respectively, if the huge L_{IR} is originated from a massive starburst. The apparent surface densities of L_{IR} and SFR, Σ_{gas} and $\Sigma_{L_{\text{IR}}}$, of the unresolved compact component are similar to those of local ULIRGs cores, i.e., close to the theoretically expected maximum value imposed by the Eddington limit, although a constraint is required on the magnification factor (if any) to yield further quantitative discussions.

ACKNOWLEDGMENTS

We would like to thank everyone who helped staff and support the AzTEC/ASTE 2008 operations and data calibration, including N. Ukita, M. Tashiro, M. Uehara, S. Doyle, P. Horner, J. Cortes, J. Karakla, and G. Wallace. The ASTE project is driven by the Nobeyama Radio Observatory (NRO), a branch of the National Astronomical Observatory of Japan (NAOJ), in collaboration with the University of Chile and Japanese institutions including the University of Tokyo, Nagoya University, Osaka Prefecture University, Ibaraki University, and Hokkaido University. Partial observations with ASTE were carried out remotely from Japan using NTT's GEMnet2 and its partner R&E networks, which are based on the AccessNova collaboration of the University of Chile, NTT Laboratories, and the NAOJ. This study was supported in part by the MEXT Grant-in-Aid for Specially Promoted Research (No. 200001003). The Submillimeter Array is a joint project between the Smithsonian Astrophysical Observatory and the Academia Sinica Institute of Astronomy and Astrophysics and is funded by the Smithsonian Institution and the Academia Sinica. Support for CARMA construction was derived from the Gordon and Betty Moore Foundation, the Kenneth T. and Eileen L. Norris Foundation, the James S. McDonnell Foundation, the Associates of the California Institute of Technology, the University of Chicago, the states of California, Illinois, and Maryland, and the National Science Foundation. Ongoing CARMA development and operations are supported by the National Science Foundation under a cooperative agreement, and by the CARMA partner universities.

REFERENCES

- Amblard, A., et al. 2010, *A&A*, 518, 9
 Arétxaga, I., et al. 2003, *MNRAS*, 342, 759
 Arétxaga, I., et al. 2007, *MNRAS*, 379, 1571
 Austermann, J. E., et al. 2010, *MNRAS*, 401, 160
 Barvainis, R., et al. 2002, *ApJ*, 571, 712
 Beelen, A., et al. 2008, *A&A*, 485, 645
 Bell, E. F. 2003, *ApJ*, 586, 794
 Bertoldi, F., et al. 2007, *ApJS*, 172, 132
 Biggs, A. D., & Ivison, R. J., 2008, *MNRAS*, 385, 893
 Blain, A. W. 1996, *MNRAS*, 283, 1340
 Bolzonella, M., et al. 2000, *A&A*, 363, 476
 Borys, C., et al. 2003, *MNRAS*, 344, 38
 Bradford, C. M., et al. 2009, *ApJ*, 705, 112
 Bruzual, G. & Charlot, S. 1993, *ApJ*, 405, 538
 Bruzual, G. & Charlot, S. 2003, *MNRAS*, 344, 1000
 Calzetti, D. 2000, *ApJ*, 533, 695
 Chapman, S. C., et al. 2004, *ApJ*, 611, 732
 Coleman, G. D., et al. 1980, *ApJS*, 43, 393
 Condon, J. J. 1992, *ARA&A*, 30, 575
 Coppin, K., et al. 2006, *MNRAS*, 372, 1621
 Cowie, L. L., et al. 2009, *ApJ*, 697, L122
 Cunningham, C. R., et al. 1994, *SPIE*, 2198, 638
 De Breuck, C., et al. 2003, *A&A*, 401, 911
 Devlin, M. J., et al. 2009, *Nature*, 458, 737
 Downes, D., et al. 1999, *ApJ*, 513, 1
 Downes, T. P., et al. 2011, *MNRAS*, submitted
 Dunlop, J. S., et al. 2004, *MNRAS*, 350, 769
 Dunne, L., et al. 2003, *MNRAS*, 341, 589
 Dunne, L., et al. 2009, *MNRAS*, 394, 3
 Eales, S., et al. 1999, *ApJ*, 515, 518
 Eales, S., et al. 2010, *PASP*, 122, 499
 Elmegreen, B. G., et al. 1999, *ApJ*, 517, 103
 Ezawa, H., et al. 2004, *SPIE*, 5489, 763
 Ezawa, H., et al. 2008, *SPIE*, 7012, 6
 Furusawa, H., et al. 2008, *ApJS*, 176, 1
 Gonzalez, A. H., et al. 2010, *ApJ*, 720, 245
 Greve, T. R., et al. 2004, *MNRAS*, 354, 779
 Greve, T. R., et al. 2005, *MNRAS*, 359, 1165
 Greve, T. R., et al. 2007, *MNRAS*, 382, 48
 Greve, T. R., et al. 2008, *MNRAS*, 389, 1489
 Hatsukade, B., et al. 2011, *MNRAS*, 411, 102
 Hezaveh, Y. D., & Holder, G. P., 2010, *ApJ*, 734, 52
 Holland, W. S., et al. 1999, *MNRAS*, 303, 659
 Hughes, D. H., et al. 1997, *MNRAS*, 289, 766
 Hughes, D. H., et al. 1998, *Nature*, 394, 241
 Hughes, D. H., et al. 2002, *MNRAS*, 335, 817
 Ibar, E., et al. 2010, *MNRAS*, 401, L53
 Iono, D., et al. 2006, *ApJ*, 640, L1
 Iono, D., et al. 2006, *ApJ*, 645, L97
 Ivison, R. J., et al. 2000, *MNRAS*, 315, 209
 Ivison, R. J., et al. 2008, *MNRAS*, 390, 1117
 Ivison, R. J., et al. 2010a, *A&A*, 518, 35
 Ivison, R. J., et al. 2010b, *MNRAS*, 402, 245
 Ivison, R. J., et al. 2010c, *MNRAS*, 404, 198
 Johansson, D., et al. 2010, *A&A*, 514, 77
 Kamazaki, T., et al. 2005, *ASPC*, 347, 533
 Kennicutt, R. C., Jr., 1998, *ARA&A*, 36, 189
 Knudsen, K. K., et al. 2006, *MNRAS*, 368, 487
 Kovács, A., et al. 2006, *ApJ*, 650, 592
 Kreysa, E., et al. 1998, *SPIE*, 3357, 319
 Lacy, M., 2004, *ApJS*, 154, 166L
 Laurent, G. T., et al. 2005, *ApJ*, 623, 742
 Lestrade, J. F., et al. 2010, *A&A*, 522, 4
 Lewis, G. F., et al. 2002, *MNRAS*, 330, 15
 Lima, M., et al. 2010, *ApJ*, 717, L31
 Lupu, M., et al. 2011, *ApJ*, submitted
 Maiolino, R., et al. 2009, *A&A*, 500, 1
 Matsushita, S., et al. 2009, *ApJ*, 693, 56
 Michałowski, M. J. et al. 2010, *A&A*, 514, A67
 Murphy, E. J. 2009, *ApJ*, 700, 482
 Negrello, M., et al. 2007, *MNRAS*, 377, 1557
 Negrello, M., et al. 2010, *Sci*, 330, 800
 Nishiyama, K., Nakai, N., & Kuno, N., 2001, *PASJ*, 53, 757
 Omont, A., et al. 1996, *Nature*, 382, 428
 Ouchi, M., et al. 2005, *ApJ*, 620, 10
 Papadopoulos, P. P., et al. 2000, *ApJ*, 528, 626
 Perera, T. A., et al. 2008, *MNRAS*, 391, 1227
 Pope, A., et al. 2006, *MNRAS*, 370, 1185
 Riechers, D. A., et al. 2009, *ApJ*, 703, 1338
 Sault, R. J., et al. 1995, *ASPC*, 77, 433
 Scott, K. S., et al. 2008, *MNRAS*, 385, 2225
 Scott, K. S., et al. 2010, *MNRAS*, 405, 2260
 Scoville, N. Z., et al. 1993, *PASP*, 105, 1482
 Simpson, C., et al. 2006, *MNRAS*, 372, 741
 Siringo, G., et al. 2008, *SPIE*, 7020, 2
 Smail, I., et al. 1997, *ApJ*, 490, 5
 Stevens, A., et al. 2003, *Nature*, 425, 264
 Swinbank, A. M., et al. 2010, *Nature*, 464, 733
 Tacconi, L. J., et al. 2006, *ApJ*, 640, 228

- Tamura, Y., et al. 2009, *Nature*, 459, 61
Thompson, T. A., et al. 2005, *ApJ*, 630, 167
Ueda, Y., et al. 2008, *ApJS*, 179, 124
Venturini, S., et al. 2003, *ApJ*, 590, 740
Vieira, J. D., et al. 2010, *ApJ*, 719, 763
Voss, H., et al. 2006, *A&A*, 448, 823
Wang, R., et al. 2010, *ApJ*, 714, 699
Wardlow, J. L., et al. 2010, *MNRAS*, 401, 2299
Warren, S. J., et al. 2007, *MNRAS*, 375, 213
Weiβ, A., et al. 2007, *A&A*, 467, 955
Weiβ, A., et al. 2009, *ApJ*, 707, 1201
Wilson, G. W., et al. 2008a, *MNRAS*, 386, 807
Wilson, G. W., et al. 2008b, *MNRAS*, 390, 1061
Wong, T. and Blitz, L. 2002, *ApJ*, 569, 157
Younger, J. D., et al. 2007, *ApJ*, 671, 1531
Younger, J. D., et al. 2008, *ApJ*, 688, 59
Younger, J. D., et al. 2009, *ApJ*, 704, 803
Yun, M. S., et al. 2001, *ApJ*, 554, 803